A short intrinsically disordered domain of MCPyV ALTO regulates host TBK1 signaling and MCPyV latency

Taylor E. Senay, Xiaomei Li, Sneha G. Shirhattikar, Tiana T. Luo, and Jianxin You[#]

Department of Microbiology, Perelman School of Medicine,

University of Pennsylvania, Philadelphia, PA 19104-6076

Running Title: ALTO disordered domain mediates viral latency via TBK1

[#]Correspondence to Jianxin You, jianyou@pennmedicine.upenn.edu

Word count for the abstract: 249

Word count for the text: 5278

Abstract:

Merkel Cell Polyomavirus (MCPyV) is an oncogenic human polyomavirus that latently infects most adults. Although the causative link between MCPyV and Merkel Cell Carcinoma (MCC) is well established, the molecular mechanisms that govern viral latency and prevent oncogenic progression remain poorly understood. We previously reported that the MCPyV early region protein ALTO is a key modulator of the STING-TBK1 signaling axis, enabling the virus to co-opt host innate immune pathways to suppress excessive viral replication and promote latency over transformation. In this study, we expand on this model by identifying a short, essential domain within ALTO that is required for TBK1 activation. This domain, which we term LIT (Lost in Tau), is necessary for ALTO-TBK1 interaction but dispensable for ALTO trafficking and its interactions with STING or Src. When expressed alone, the LIT domain functions as a dominant negative inhibitor of wild-type ALTO, competitively blocking TBK1 activation through a novel TBK1 interaction domain. Deletion of the LIT domain from ALTO not only abolishes TBK1 interaction and downstream phosphorylation but also eliminates TBK1-mediated suppression of MCPyV replication during early infection of human dermal fibroblasts (HDFs). These findings provide mechanistic insight into how ALTO promotes viral persistence and immune evasion. More broadly, they highlight the functional importance of intrinsically disordered regions in modulating host–virus interactions and suggest that MCPyV latency is actively maintained through a finely tuned balance of pro- and anti-viral signaling. Targeting domains such as LIT may offer new strategies for regulating TBK1 activity or disrupting viral persistence.

Importance:

Merkel cell polyomavirus causes lifelong, latent infections in the skin of most people. When this latency is perturbed, the virus can give rise to Merkel Cell Carcinoma, an aggressive and

difficult-to-treat skin cancer. Efforts to prevent this cancer depend on understanding what controls viral latency and persistence. We previously reported that MCPyV stimulates the host's STING-TBK1 signaling axis to limit its own replication. In this work, we identify and characterize a short amino acid motif within the ALTO protein's intrinsically disordered region that is required for this immune-stimulating activity. This region appears to be critical for helping the virus maintain latency by fine-tuning the host's response. Our findings provide new insight into MCPyV's latency mechanism and may help guide future approaches to prevent or treat Merkel cell carcinoma by targeting viral or cellular factors involved in long-term infection.

Introduction

The viral family *Polyomaviridae* includes approximately 117 species of non-enveloped viruses carrying small (~5 kb) circular double-stranded DNA genomes(1). Of these, around 16 are thought to be human-specific(2), and only one, Merkel cell polyomavirus (MCPyV or MCV), has been conclusively demonstrated to be carcinogenic(3). MCPyV is ubiquitous in the human population and, for most individuals, exists as a silent member of the skin virome, establishing lifelong episomal latency in cutaneous cells(4-8). However, in a subset of cases, MCPyV integrates into the host genome, where it drives oncogenesis of the rare but aggressive neuroendocrine skin cancer Merkel cell carcinoma (MCC) through constitutive high-level expression of its Small Tumor (sT) antigen and a truncated form of its Large Tumor (LT) antigen(3, 9, 10).

Nearly two decades after its discovery as the major causative agent in approximately 80% of MCCs(3, 11, 12), most mechanistic studies of MCPyV have focused on LT and sT. These viral effectors have homologs in other well-characterized polyomaviruses, such as SV40, and their roles in MCPyV replication and transformation are well established(13-15). However, the

upstream events that initiate viral genome truncation and integration, as well as the cellular conditions that distinguish persistent infection from oncogenic progression, remain poorly understood. These represent critical gaps in our knowledge of MCPyV biology. Elucidating the regulatory mechanisms that govern this transition is essential for improving early detection and prevention of MCC, which currently has limited and often non-durable treatment options.

There is currently no consensus on how MCPyV establishes, maintains, or exits latency. Clinical observations reveal that immunosuppressed individuals carry higher MCPyV viral burdens and are at substantially increased risk of developing MCC, suggesting that innate immune control is a key determinant of viral latency(16-18). The cyclic GMP-AMP synthase–stimulator of interferon genes (cGAS–STING) pathway, a cytosolic DNA-sensing system that activates type I interferon and proinflammatory signaling, has emerged as particularly important in this context(19-25). We have previously reported that STING expression is dramatically reduced in virus-positive MCC tumors, and that reactivation of STING signaling promotes MCC cell death and T-cell infiltration(26). Conversely, during early infection, MCPyV strongly activates the STING pathway and its downstream proinflammatory effectors, which in turn restricts viral replication and supports the establishment of a balanced, persistent infection(27-29). Together, these findings suggest that MCPyV latency is not a passive process, but rather one that is tightly regulated through interactions between viral effectors and host innate immune pathways. Disruption of this equilibrium, whether through viral mutation or host immune suppression, may be a critical inflection point that drives malignant progression.

While LT and sT have been the primary focus of MCPyV research, less attention has been paid to another early region protein, the Alternative Large Tumor antigen open reading frame (ALTO). First identified in 2014, ALTO was initially thought to be dispensable for replication in transfection-based assays(30). However, recent studies, including our own, have revealed its

active role in immune signaling. ALTO has been shown to modulate Src-family kinases, PLCγ1 signaling(31), and the NFκB pathway(31, 32). In our recent work, we demonstrated that ALTO acts as a modulator of the STING–TBK1 axis, forming a signaling complex with STING, TBK1, and Src to induce TBK1 autophosphorylation, leading to its degradation and resulting in viral replication suppression and latency promotion(29). This function places ALTO in the unique position of acting as an “anti-viral viral protein” that dampens its own replication evade immune detection and persist in the host.

These findings reshape our understanding of ALTO as a multifunctional effector in MCPyV biology, one that fine-tunes host responses through structurally flexible, context-dependent interactions. In this study, we build upon our prior work to dissect the structure-function relationship of ALTO in greater detail. Using a systematic truncation approach, we identify a short, previously uncharacterized region within ALTO’s intrinsically disordered domain that is required for its interaction with TBK1 and its immunomodulatory function. Through this analysis, we aim to illuminate how ALTO contributes to latency maintenance, how disruption of its function may promote oncogenesis, and how ALTO-targeted mechanisms could be leveraged to better understand or intervene in MCPyV-associated disease.

Results

Identification of the TBK1-activating domain within ALTO’s N-terminal intrinsically disordered region

As shown in our previous study published in 2024, one of ALTO’s key features is its ability to stimulate TBK1 autophosphorylation(29). To identify the region(s) of ALTO responsible for stimulating TBK1 autophosphorylation, we began by evaluating the current understanding of ALTO’s structural features. The ALTO protein remains poorly characterized at the structural

116 level, and even its precise length is debated: while early studies described a 250-amino acid
117 (aa) product encoded across two exons, more recent annotations favor a 248-aa version
118 encoded within a single exon(30-32). As no conclusive functional differences between these
119 isoforms have been reported, we included both in our *in vitro* studies and observed no
120 phenotypic distinctions between them.

121 Multiple reports of *in silico* analyses agree that ALTO's most stable structural feature is a C-
122 terminal alpha helix (approximately aa 200-250) that contains a 22-aa transmembrane or
123 hydrophobic domain (aa 225-246). In contrast, the N-terminal region, representing roughly 80%
124 of the protein, is intrinsically disordered (Fig. 1A)(33-35). Although intrinsically disordered
125 regions (IDRs) are known to be highly plastic and capable of a wide range of functions(36-39)
126 their lack of fixed globular shape makes structure-based functional prediction based on
127 modeling difficult. We therefore took a methodical but exploratory approach using progressive
128 N-terminal focused truncation. Each truncation shortened the protein by 30-aa compared to the
129 one before, allowing us to examine region-specific phenotypic variation with fine resolution (Fig.
130 1B). In addition to the progressive N-terminal truncation mutants, we constructed a C-terminal
131 ALTO truncation variant lacking the hydrophobic or transmembrane domain (ALTOΔTM). These
132 variant sequences were generated using the NanoBiT platform, a structural complementation-
133 based split enzyme system which quantifies tagged protein-protein interactions in live cells via
134 relative luminescence. We have previously found that ALTO favors N-terminal functional
135 tags(29), so all constructs were generated with N-terminal LgBiT and SmBiT tags—the large
136 and small subunits, respectively, of a reconstitutable NanoLuc luciferase enzyme—enabling
137 protein detection and downstream protein-protein interaction analysis (Fig. 1B).

138 To test which region or regions of ALTO govern its TBK1-stimulatory activity, we transfected
139 HEK 293T cells with constructs encoding LgBiT-tagged ALTO progressive truncation mutants or
140 an empty vector control. Expression of most variants was roughly equivalent, and all migrated to

141 positions consistent with their predicted molecular weights (Fig. 1C). Although structural
142 prediction of ALTO remains largely inconclusive, AlphaFold modeling suggested that all variants
143 preserved the characteristic N-terminal disordered region and C-terminal alpha helix (Fig. S1).
144 Since ALTO is also known to form homo-oligomers(29, 31), we used ALTO-ALTO interactions as
145 a functional readout to assess the structural integrity of the truncation mutants. Self-interaction
146 assays confirmed that variants retained appropriate homo- and hetero-oligomerization capability
147 (Fig. S2), further supporting the functional integrity of these constructs.

148 We then tested whether the ALTO truncation mutants retained the ability to stimulate TBK1
149 autophosphorylation. As observed with wildtype (WT) ALTO, the first four truncation mutants
150 (ALTOΨ, ALTOχ, ALTOΦ, and ALTOυ) retained the ability to stimulate TBK1
151 autophosphorylation (Fig. 1C, lanes 1-5). In contrast, the ALTOτ truncation (aa 151–250) and all
152 shorter N-terminal truncated variants completely lost this activity despite comparable protein
153 expression levels (Fig. 1C, lane 6-8). ALTOΔTM also failed to stimulate TBK1
154 autophosphorylation and was expressed at a relatively lower level (Fig. 1C, lane 9). This, taken
155 with its overall lowered homo- and hetero-oligomerization capability (Fig. S2) supports previous
156 reporting that the putative transmembrane or hydrophobic domain is required for robust
157 expression of ALTO(32).

158

159 **The LIT domain is specifically required for ALTO-TBK1 interaction but not for binding**
160 **STING or Src**

161 The loss of TBK1 autophosphorylation in ALTOτ and shorter variants may indicate a disruption
162 in the formation of the ALTO-STING-TBK1-Src “signal complex” we previously described(29). To
163 determine whether the loss of TBK1-stimulatory activity in certain truncation mutants was due to
164 disrupted complex formation—and to identify which specific protein-protein interactions might

165 underlie the observed loss of function—we co-transfected HEK 293T cells with SmBiT-tagged
166 ALTO truncation mutants and LgBiT-tagged STING, TBK1, or Src (Fig. 2A-C). Kinetic monitoring
167 of these interactions showed that after a short equilibration period, all readings remained
168 relatively stable over the observation window; therefore, single representative timepoints are
169 presented throughout this study (Fig. S3). For all three interactors, interaction strength was
170 substantially reduced or eliminated at different truncation points, suggesting that STING, Src,
171 and TBK1 each rely on distinct ALTO regions for binding.

172 Despite its inability to stimulate TBK1 autophosphorylation as we observed in Fig. 1C, ALTOτ
173 showed the strongest interaction with STING (Fig. 2A) and retained approximately half-maximal
174 interaction with Src (Fig. 2B), indicating it remains structurally and functionally competent in
175 other respects. ALTO-TBK1 interaction peaked with the ALTOΦ variant, declined substantially
176 with ALTOυ, and was reduced to near-background levels at ALTOτ (Fig. 2C). These data
177 suggest that ALTOτ is properly folded and localized but lacks a domain specifically required for
178 ALTO-TBK1 engagement. Taken together, the TBK1 activation and protein-protein interaction
179 assays identify the 30aa region absent in ALTOτ (aa 121-150) as a critical functional segment.
180 We therefore refer to this region as the Lost in Tau (LIT) domain.

181

182 **The LIT domain functions as a dominant negative inhibitor of ALTO-induced TBK1**
183 **autophosphorylation**

184 To further investigate whether the LIT region is sufficient to confer TBK1-related activity, we
185 tested whether the domain alone could recapitulate or inhibit full-length ALTO function. We first
186 cloned the LIT sequence into the NanoBiT vectors for use in sensitive live cell interaction
187 assays, then subcloned the same reading frame with the addition of the N-terminal LgBiT tag

188 into the pcDNA4c vector, adding an Xpress tag and placing the construct under the control of a
189 highly active CMV promoter for applications requiring more robust expression (Fig. 3A).

190 NanoBiT protein-protein interaction studies of LIT's interactions with wild-type (WT) ALTO,
191 STING, Src, and TBK1 were initiated using the standard LgBiT-LIT construct; however, we
192 observed substantial differences in expression levels between WT ALTO and LIT, as well as
193 high variability and background luminescence readings in both experimental and negative
194 control conditions (Fig. S4). Because higher LIT expression would also produce proportionally
195 higher background signal, we concluded that the NanoBiT platform was not suitable for reliably
196 examining LIT interactions.

197 Since the LIT domain appeared to be critical for ALTO-TBK1 interactions (Figs. 1C, 2C), we
198 hypothesized that it might act as a dominant negative inhibitor by competitively interfering with
199 TBK1 activation by WT protein. To test this, we co-transfected our Xpress-LgBiT-LIT construct
200 with WT ALTO and assessed TBK1 autophosphorylation as well as total TBK1 protein levels. As
201 expected, modest expression of WT ALTO alone strongly stimulated TBK1 autophosphorylation,
202 whereas even much higher expression of Xpress-LgBiT-LIT failed to do so (Fig. 3B). Co-
203 transfection of the two constructs showed a marked decrease in TBK1 autophosphorylation,
204 confirming a dominant negative phenotype.

205 An alternate ALTO mutant containing the N-terminal 150 aa of ALTO—terminating with the LIT
206 region—was tested as a more stable truncation construct than LIT alone, without requiring a
207 bulky N-terminal tag (Fig. S5). This variant, termed ALTO150, was stably and detectably
208 expressed; however, it had only a modest inhibitory effect on TBK1 autophosphorylation when
209 co-transfected with WT ALTO. Co-transfection also resulted in a modest increase in WT ALTO
210 abundance, suggesting that the N-terminal domain of ALTO mediates its dimerization, which in
211 turn contributes to protein stabilization. While ALTO150 exhibited some dominant negative

212 activity, its stabilization of WT ALTO may offset this effect, creating a self-limiting interaction that
213 blunts its ability to fully suppress WT ALTO function.

214

215 **Deletion of the LIT domain abolishes TBK1 activation without disrupting ALTO structure,**
216 **oligomerization, or other partner binding**

217 While truncation mutants helped define the boundaries of the LIT domain, we next asked
218 whether targeted deletion of this region would phenocopy the loss of function seen in ALTOτ. To
219 determine whether the observed loss of interaction and TBK1 stimulation was due to a
220 sequence-specific function of the LIT region or simply a consequence of reduced length or
221 flexibility, we generated an ALTO variant lacking the LIT coding sequence, termed ALTO deletion
222 of LIT (ALTOdelLIT) (Fig. 4A). The removal of a random 30aa segment was not expected to
223 produce a phenotype, as a deletion of this length in the ALTOΨ truncation did not impair TBK1
224 autophosphorylation or interaction (Figs. 1C, 2C).

225 Consistent with previous results, LgBiT-tagged WT ALTO robustly stimulated TBK1
226 autophosphorylation and degradation in transfected HEK 293T cells. In contrast, ALTOdelLIT
227 failed to induce either autophosphorylation or degradation of TBK1, despite comparable protein
228 expression levels (Fig. 4B). NanoBiT interaction assays confirmed that this loss of function was
229 not due to impaired ALTO oligomerization, as ALTOdelLIT retained equal or even enhanced
230 capability to oligomerize with itself and with WT ALTO (Fig. 4C). Similarly, interactions between
231 ALTOdelLIT and STING (Fig. 4D), as well as ALTOdelLIT and Src (Fig.4E), were not
232 significantly different from those of WT ALTO. Interaction between ALTOdelLIT and TBK1,
233 however, was reduced by more than 30-fold compared to WT ALTO (Fig. 4F), indicating a
234 specific requirement for the LIT region in TBK1 engagement. Protein expression across all
235 interaction assays was largely equal, further supporting the reliability of these findings (Fig. S6).

236 The preserved interactions between ALTOdelLIT and ALTO, STING, and Src suggest that
237 ALTOdelLIT is structurally and functionally intact, and that its loss of TBK1 engagement reflects
238 a specific requirement for the LIT region.

239 The LIT region lies within ALTO's N-terminal intrinsically disordered region (IDR), and as such,
240 no confident structure-based predictions can be made about its function or (Fig. 1A). To further
241 investigate whether specific functional domain(s) of ALTO within the LIT region might drive the
242 ALTO-TBK1 interaction, we analyzed its amino acid sequence for short linear motifs (SLiMs),
243 also known as eukaryotic linear motifs (ELMs), using the ELM Resource prediction tool
244 (http://elm.eu.org/search.html). The analysis was performed without specifying a subcellular
245 compartment, as ALTO's subcellular localization remains poorly defined. The resulting
246 predictions were then filtered to include only those located within or adjacent to the LIT region
247 (Fig. S7). Although SLiMs are inherently degenerate and therefore not considered high-
248 confidence predictions when found, no motifs corresponding to known TBK1-binding sites or
249 interaction domains with other signal complex components were identified.

250

251 **The LIT domain does not influence ALTO subcellular localization or trafficking**

252 Given that ALTOdelLIT retains structural integrity and continues to interact with Src, STING, and
253 itself, we next hypothesized that differences in intracellular trafficking might account for the
254 phenotypic divergence between WT ALTO and ALTOdelLIT. To test this, we generated human
255 dermal fibroblasts (HDFs) expressing either WT ALTO or ALTOdelLIT under a doxycycline (Dox)
256 inducible promoter (inALTOWT and inALTOdelLIT HDFs, respectively). After several hours of
257 Dox induction, cells were fixed and immunostained for ALTO and various intracellular membrane
258 markers. Substantial colocalization was observed only with the cis-Golgi marker GM130, where
259 both WT ALTO and ALTOdelLIT appeared to accumulate during early expression (Fig. 5A). At

later time points, both proteins were observed to traffic outward from the Golgi, potentially via the secretory pathway (Fig. S8). Further immunofluorescence analysis revealed partial colocalization of distal ALTO and ALTOdelLIT foci with the early endosome marker Rab5 (Fig. 5B), suggesting ALTO may transiently localize to the plasma membrane and re-enter the cell via the endocytic pathway, a finding consistent with prior reports of ALTO co-fractionating with lipid raft markers(31).

Although we did not identify a specific motif or altered trafficking pattern that could explain the loss of ALTO-TBK1 interaction in the absence of the LIT domain, these findings suggest that ALTO's trafficking may involve dynamic cycling through the secretory and endocytic pathways. Further investigation into ALTO's trafficking and intracellular lifecycle may provide important insights. Despite the absence of clear structural or localization changes, our data demonstrate that the LIT domain is specifically required for ALTO-induced TBK1 autophosphorylation.

The LIT domain is essential for ALTO-mediated suppression of MCPyV replication in infected cells

Finally, to place our protein-level observations into their full viral context, we evaluated whether WT ALTO and ALTOdelLIT could suppress MCPyV replication by using our HDF model of early MCPyV infection(40). Donor-matched inALTOWT and inALTOdelLIT HDFs (Fig. 6A) were infected with equal titers of $ALTO_{null}$ MCPyV, a genetically intact virus containing a point mutation in the ALTO start codon that eliminates ALTO expression(29). Following infection, cells were either mock-induced or induced to express their respective ALTO variant, and viral replication was assessed five days post-infection.

As we previously reported, $ALTO_{null}$ virus replicates significantly more efficiently in uninduced HDFs compared to HDFs induced to express WT ALTO. In contrast, induction of ALTOdelLIT

284 failed to significantly reduce viral replication (Fig. 6B). Because the suppression of viral
285 replication by ALTO is known to occur through a TBK1-driven negative feedback
286 mechanism(29), this loss of function demonstrates that the LIT domain is required for TBK1
287 stimulation by ALTO during viral infection.

288

289 **Discussion**

290 MCPyV remains the only conclusively identified oncogenic human polyomavirus. Despite its
291 widespread presence in the general population and its clear role in the pathogenesis of MCC,
292 major gaps persist in our understanding of key aspects of MCPyV biology. Among the most
293 critical of these are the mechanisms by which MCPyV establishes persistent infection, maintains
294 latency, and ultimately exits latency to drive oncogenesis.

295 This study builds on our previous work proposing an MCPyV latency mechanism involving
296 ALTO-mediated modulation of the STING–TBK1 axis. To further define this mechanism, we
297 used a progressive N-terminal truncation approach spanning ALTO's intrinsically disordered
298 region (IDR) and alpha-helical domain to identify regions critical for TBK1 activation (Figs. 1A,
299 1B). Through this strategy, we discovered a short, previously uncharacterized region of ALTO
300 that is specifically required for TBK1 stimulation. The ALTOτ mutant, which retains only the C-
301 terminal 100 amino acids of ALTO (aa 151–250), was the first truncation to completely lose the
302 ability to stimulate TBK1 autophosphorylation in cellulo (Fig. 1C) and showed almost no
303 detectable interaction with TBK1 in protein–protein interaction assays (Fig. 2C). In contrast, its
304 immediate upstream predecessor, ALTOυ, retained both activity and binding, indicating that the
305 30 amino acids present in ALTOυ but absent in ALTOτ (aa 121–150) are essential for this
306 function. We therefore designated this region the LIT (Lost in Tau) domain. Located within

307 ALTO's IDR, the LIT domain is predicted to localize at the interface of ALTO, STING, TBK1, and
308 Src within the multi-protein signal complex (Fig. 6C).

309 When expressed in isolation, the LIT domain acted as a dominant negative inhibitor of WT
310 ALTO, competitively blocking TBK1 activation (Fig. 3B). To confirm that the LIT domain is
311 necessary for ALTO's immune modulatory activity, we engineered a deletion construct
312 (ALTOdelLIT) and found that it failed to stimulate TBK1 autophosphorylation (Fig. 4B). This loss
313 of function appears to be sequence-specific: ALTOdelLIT maintained expression, proper folding,
314 and interactions with other signal complex proteins such as STING and Src, but showed a
315 dramatic reduction in TBK1 binding (Fig. 4F). This loss was not attributable to the absence of a
316 canonical TBK1-interaction motif (Fig. S7) or to altered protein trafficking, as ALTO and
317 ALTOdelLIT both localized to the cis-Golgi at early time points and trafficked through both the
318 secretory and endocytic pathways (Figs. 5A, 5B).

319 Finally, we demonstrated that the LIT domain is functionally required for TBK1-mediated
320 suppression of MCPyV replication during early infection (Fig. 6A). Notably, ALTOdelLIT
321 induction failed to reduce viral replication to the extent observed with direct pharmacological
322 inhibition of TBK1(29) in our prior study. These results support the conclusion that ALTO,
323 through the LIT domain, plays a central role in modulating host–virus interactions during both
324 early and persistent infection.

325 The identification of a novel immune interaction domain within ALTO's IDR builds on prior
326 reports implicating other regions of ALTO in Src-family kinase binding(29, 31), PLCγ1 signaling,
327 and NFκB modulation(31, 32). Collectively, these studies revise the earlier view of ALTO as a
328 dispensable accessory protein and instead establish it as a key viral effector that actively
329 shapes innate immune responses through structurally dynamic interactions. As ALTO-encoding
330 polyomaviruses continue to emerge as a phylogenetic subset of mammalian
331 polyomaviruses(32), it will be important to assess whether the LIT domain is conserved across

species or represents a specialized adaptation of MCPyV to its human host. Given that many polyomaviruses establish persistent infections, conservation of LIT-like motifs would support the idea that latency is a regulated process driven by active host–virus interactions, rather than a passive consequence of viral quiescence.

MCPyV ALTO is not unique among viral or oncogenic proteins in its use of intrinsic disorder to regulate complex signaling networks. Other viral effectors, including HPV E7(41) and KSHV ORF57(42), also use disordered regions to engage host pathways with high flexibility and specificity. As the functional importance of intrinsically disordered viral proteins becomes more widely appreciated, new opportunities are emerging to map these regions and understand their mechanistic roles in immune evasion, persistence, and oncogenesis(43-45).

Several key questions remain regarding the lifecycle and regulation of ALTO during MCPyV infection. Although we observed initial accumulation of ALTO at the cis-Golgi, followed by trafficking through secretory and endocytic pathways (Figs. 5, S8), and prior studies have reported association with lipid rafts(31), the complete subcellular dynamics of ALTO, particularly during long-term infection, are not yet well defined. Given the known importance of spatial regulation for many signaling proteins, a deeper understanding of ALTO's localization and trafficking may reveal new insights into its diverse functions and regulatory partners.

A particularly intriguing and unresolved observation is the frequent loss of ALTO expression in virus-positive MCC, even in cases where the ORF is retained(32). While some loss may result from stochastic truncation events during viral integration, ALTO protein is undetectable in several virus-positive MCC lines that retain its intact coding sequence. From an evolutionary perspective, this may be a form of immune evasion. ALTO is highly immunostimulatory, and its continued expression after integration could trigger immune clearance of the host cell. Thus, the absence of ALTO in MCC tumors may reflect a form of survivorship bias. Only those cells that have lost ALTO expression may escape immune detection and progress to cancer. Since ALTO

357 can be robustly expressed even in the absence of all other viral proteins, this suggests that
358 host-mediated regulatory mechanisms, rather than viral factors, may suppress ALTO post-
359 integration. Identifying such factors could reveal novel therapeutic targets or biomarkers for
360 MCC progression.

361 Finally, the discovery of a compact domain within ALTO that selectively activates TBK1 opens
362 the door to potential translational applications. ALTO itself or a small molecule mimic of its TBK1
363 activating domain could serve as a noncanonical TBK1 agonist for boosting antiviral immunity in
364 immunocompromised individuals, potentially suppressing MCPyV replication and reducing
365 cancer risk. Beyond direct antiviral applications, TBK1 is a known druggable target for a variety
366 of conditions associated with its dysregulation, as well as a target of interest in the development
367 of novel cancer immunotherapies(46-48). Identification and characterization of the noncanonical
368 mechanism by which ALTO is able to stimulate TBK1 autophosphorylation could also enable the
369 development of novel agonists and antagonists. Conversely, the LIT domain itself, or derivatives
370 thereof, could act as dominant negative inhibitor of WT ALTO by blocking its ability to activate
371 TBK1. This raises the possibility of repurposing LIT-mimicking compounds to modulate ALTO-
372 TBK1 signaling in MCPyV-associated conditions, such as latency control or early-stage
373 infection.

374

375 **Materials and methods**

376 Cell culture

377 All cells were maintained at 37°C with 5% CO_2 in a humidified incubator. HEK 293T cells were
378 cultured in Dulbecco's Modified Eagle Medium (DMEM, Gibco) supplemented with 10% fetal
379 bovine serum (FBS, Cytiva). HDFs were isolated from neonatal foreskin as previously

380 described(49) and maintained in DMEM supplemented with 10% tetracycline-screened FBS
381 (Cytiva).

382

383 Chemicals and reagents

384 Doxycycline (Dox) and puromycin were dissolved in sterile water to stock concentrations of 0.5
385 mg/mL and 10 mg/mL, respectively, and stored at −20°C. Unless otherwise noted in the text or
386 figure legends, Dox was used at a final concentration of 0.5 μg/mL. Puromycin was used during
387 selection for stable cell lines as described below. Hexadimethrine bromide (Polybrene, Aldrich)
388 was dissolved in water to a 12 mg/mL stock, sterilized by 0.2 μm syringe filtration, and used
389 fresh for each experiment.

390

391 Recombinant plasmid construction

392 NanoBiT constructs expressing WT ALTO, TBK1 and STING were generated in our previous
393 study(29). The human c-Src coding sequence (hereafter “Src”) was amplified from the
394 pDEST40-ZXHA-WtSrc plasmid and cloned using XhoI and NheI sites. LgBiT- and SmBiT-
395 tagged truncated ALTO mutants (Ψ, χ, Φ, υ, τ, σ, ρ, ΔTM, and LIT) were PCR-amplified from the
396 pBiT1.1-N_ALTO (L-ALTO) backbone and subcloned into pBiT1.1-N[TK/LgBiT] or pBiT2.1-
397 N[TK/SmBiT] vectors using XhoI and NheI.

398 Deletion constructs pBiT1.1-N_ALTOdelLIT (L-ALTOdelLIT) and pBiT2.1-N_ALTOdelLIT (S-
399 ALTOdelLIT) were constructed by linear PCR omitting the LIT region, followed by Bpu10I
400 digestion and self-ligation.

401 Constructs for pcDNA4c-ALTO150 and pcDNA4c-LgBiT-LIT were prepared by amplifying their
402 respective coding sequences from their respective NanoBiT plasmids and subcloning into the
403 pcDNA4c vector (Invitrogen) using BamHI and XhoI or EcoRI, respectively.

404 The pTRIPz-RFP vector (Open Biosystems) and pTRIPz-ALTO construct were generated as
405 previously described(29). pTRIPz-ALTOdelLIT was derived from pBiT1.1-N_ALTOdelLIT and
406 cloned into the pTRIPz backbone using the AgeI and MluI sites to replace the RFP cassette. All
407 primer sequences are provided in Supplemental Table 1.

408

409 Structural prediction

410 Structural modeling of WT ALTO (Fig. 1A) was performed as previously described(29, 35).
411 Progressive ALTO truncation mutants and the STING-TBK1-ALTO-Src complex were modeled
412 using the AlphaFold3 server (builds 2025.5.23 and 2025.06.10) with default settings(34). Models
413 were visualized and recolored using NIH iCn3D(50, 51).

414

415 Generation of inducible stable HDFs

416 Inducible HDF lines were generated as previously described(27, 49). Briefly, lentiviral particles
417 were produced in HEK 293T cells by co-transfecting pTRIPz transfer plasmids (encoding WT
418 ALTO or ALTOdelLIT), psPAX, and pMD2.G using Lipofectamine 2000 (Invitrogen).
419 Supernatants were collected 48 h post-transfection, centrifuged, 0.2 μm filtered, and
420 supplemented with 6 μg/mL Polybrene prior to transduction of early-passage HDFs (≤2
421 passages post-isolation). After 48 h, media was replaced, and cells were selected with 4 μg/mL
422 puromycin for 5 days, followed by maintenance in 1 μg/mL puromycin.

423

424 NanoBiT protein–protein interaction assays

425 HEK 293T cells were seeded into opaque white 96-well plates (3×10^4 cells/well) in 100 µL
426 DMEM + 10% FBS. Warm PBS was added to outer wells and between wells to reduce edge
427 effects. The following day, cells were transfected with 100 ng total plasmid DNA per well (50 ng
428 each of LgBiT and SmBiT constructs or SmBiT control) using FuGENE HD (Promega) in Opti-
429 MEM I (Gibco). After 20–24 h incubation (20 h for TBK1 assays), media was replaced with fresh
430 Opti-MEM I ~30 min before reading. NanoGlo Live Cell Substrate (Promega) was diluted to 5X
431 in Live Cell Buffer and added under low-light conditions. Luminescence was measured using a
432 Luminoskan Ascent (Thermo) every 15 minutes for 90 minutes. Representative timepoints were
433 selected based on signal strength and stability.

434

435 Western blotting

436 Cells were lysed in ice-cold buffer (10 mM HEPES pH 7.5, 500 mM NaCl, 1 mM EDTA, 1 mM
437 DTT, 0.5% Triton X-100) supplemented with PhosSTOP (Roche) and cOmplete protease
438 inhibitors (Roche). Lysis proceeded on ice for 30–60 min with intermittent vortexing. Lysates
439 were cleared by centrifugation at 12,000 × g for 10 min at 4°C. Protein concentration was
440 determined by Bradford assay. Samples were mixed with Laemmli buffer, boiled for ≥2 min,
441 flash frozen, and stored at −80°C. Proteins were resolved by SDS-PAGE and transferred to 0.45
442 µm PVDF membranes. Blots were blocked and incubated overnight at 4°C with primary
443 antibodies diluted in 5% milk in PBST (0.1% Tween-20), followed by secondary antibodies for 1
444 h at room temperature. Signal was developed using SuperSignal West Pico PLUS (Thermo)
445 and imaged on an Amersham Imager 600 or 680 (GE Healthcare). Primary antibodies: anti-
446 GAPDH (1:5,000, CST 2118S), anti-TBK1 (1:1,000, CST 3504S), anti-phospho-TBK1 S172
447 (1:1,000, CST 5483S), anti-ALTO (1:10,000, courtesy of the Galloway Lab), anti-STING

448 (1:1,000, CST 13647S), anti-LgBiT (1:500, Promega N710A), anti-Xpress (1:1,000, Invitrogen
449 44-0528), anti-Src (1:1,000, CST 2109S). Secondary antibodies: HRP-conjugated anti-rabbit
450 IgG (1:2,500, CST 7074S), anti-mouse IgG (1:2,500, CST 7076S).

451

452 Immunofluorescent staining

453 HDF-inALTO and -inALTOdelLIT cells were seeded on coverslips and treated with Dox (0.5
454 µg/mL) for durations indicated in the figures. Cells were fixed in 3% paraformaldehyde (PBS, 20
455 min), permeabilized in 0.5% Triton X-100 / 3% BSA (1 h, RT), and incubated with primary
456 antibodies in the same buffer for 1 h in humidified chambers. Following PBS washes, secondary
457 antibodies with DAPI were applied under low-light conditions. Cells were imaged using an
458 Olympus IX81 inverted microscope. Primary antibodies: anti-ALTO (1:1,000, courtesy of the
459 Galloway Lab), anti-Rab5 (1:200, CST 3547T), anti-GM130 (1:200, BD 610822). Secondary
460 antibodies: AlexaFluor 594-conjugated goat anti-rabbit IgG (1:500, Invitrogen A11012),
461 AlexaFluor 488-conjugated goat anti-mouse IgG (1:500, Invitrogen A11029).

462

463 MCPyV infection

464 Infections using $ALTO_{null}$ MCPyV were performed in HDF-inALTO and -inALTOdelLIT lines as
465 previously described(29). Viral replication was assessed by qPCR following published
466 methods(29).

467

468 Statistical analysis

469 All statistical analyses were performed using GraphPad Prism. For single comparisons,
470 unpaired two-tailed t-tests with Welch's correction were used. For multiple group comparisons,

Brown–Forsythe and Welch's ANOVA tests were applied where indicated. Significance thresholds were: $P < 0.05$ (*), $P < 0.01$ (**), $P < 0.001$ (***). Confidence intervals were set at 95%.

Supplemental Table 1:

Primer	Sequence
Src NheI F	5'- GATCGCTAGC ATG GGTAGCAACAAGAGCAAG-3'
Src XhoI R	5'-GATCCTCGAGCC GAGGTTCTCCCCGGGC-3'
ALTO NheI R	5'-CAGTGCTAGCTCAGATCTGTTGCTTGATACGATG-3'
Ψ XhoI F	5'-CAGTCTCGAGCGGTCAGGACCCCGAGTCATTG-3'
χ XhoI F	5'-CAGTCTCGAGCGGTATGGGCCCAAGC-3'
Φ XhoI F	5'-CAGTCTCGAGCGGTCTCGACCCAGTGGCC-3'
υ XhoI F	5'-CAGTCTCGAGCGGTAGAATGGCACCAGGACG-3'
τ XhoI F	5'-CAGTCTCGAGCGGTCCACAAGAGGCCAGGC-3'
σ XhoI F	5'-CAGTCTCGAGCGGTCCAAGCCCACCAAGGC-3'
ρ XhoI F	5'-CAGTCTCGAGCGGTTTGCTGTTTCTGCTCATCTTC-3'
ALTO XhoI F	5'-CAGTCTCGAGCGGTGGCCCCTGAACAGCAAG-3'
ALTOΔTM NheI R	5'-CAGTGCTAGCTCACTTTTCGGTGCGCTTCTG-3'
LIT XhoI F	5'-CAGTCTCGAGCGGTAGAAGGCACCAGGAC-3'
LIT NheI R	5'-CAGTGCTAGCTCACGGTGGGCTGCG-3'
delLIT Bpu10I F	5'-CAGTCCTGAGCCACAAGAGGCCAGG-3'
delLIT Bpu10I R	5'-CAGTGCTCAGGCAAGATTCCAGATAGAC-3'
ALTO BamHI F	5'-CAGGGATCCGGCCCACTGAACAGCAAG-3'
ALTO150/LIT XhoI R	5'-CAGTCTCGAGTCACGGTGGGCTGCG-3'
ALTOdelLIT AgeI F	5'-ACTGACCGGTACCATGGGCCCACTGAACAGC-3'
ALTOdelLIT MluI R	5'-TGTCACGCGTTCATTGCTTGATAACGATGTAGAGC-3'
LgBiT-LIT BamHI F	5'-CAGTGGATCCATGGTCTTCACACTCGAAG-3'
LgBiT-LIT EcoRI R	5'-CAGTGAATTCTCACGGTGGGCTGC-3'

Acknowledgments

481 We thank Dr. Denise Galloway for generously providing the anti-ALTO antibody. We are also
482 grateful to the members of our laboratories for their insightful discussions and ongoing support.
483 This work was supported by the National Institutes of Health through Grants R01CA187718,
484 R21CA267803, and R01CA284690 awarded to J.Y., as well as by the National Cancer Institute
485 through P01CA281867 Project 3 to J.Y.. The funders had no role in study design, data
486 collection, interpretation, or submission for publication.
487

488 **Figure Legends**

489

490 **Figure 1: Progressive N-terminal truncation reveals ALTO functional regions.** (A)
491 Predicted tertiary structure model of ALTO (AlphaFold2 Colab) with truncation mutant lengths
492 highlighted. Chain colors correspond to the maximum N-terminal length of their respective
493 mutant, with each mutant consisting of its own color portion and all subsequent C-terminal
494 portions. (B) Schematic diagram of LgBiT- and SmBiT- (L/S) tagged progressive N-terminal
495 ALTO truncation mutants. The hydrophobic or transmembrane (TM) domain is indicated as
496 “HD”. (C) Western blots of HEK 293T lysates collected 24 hours post-transfection with 2ug of
497 the indicated LgBiT-tagged progressive ALTO truncation mutant (or an empty vector control, V).
498 Primary antibodies are listed on the right.

499 **Figure 2: ALTOT is markedly deficient in TBK1 interaction.** (A-C) Luminescence readings of
500 HEK 293T cells transfected with pairs of plasmids carrying NanoBiT-tagged ALTO progressive
501 truncation mutants and either (A) STING, (B) Src, and (C) TBK1, or the Small BiT negative
502 control construct (NC). Readings were taken at 20 hours (ALTO-TBK1) or 24 hours (ALTO-
503 STING and ALTO-Src) post-transfection. Points indicate biological replicate wells, bars indicate
504 means, and error bars indicate standard deviations. L-protein and protein-S (and similar)

505 indicate the named protein tagged with the LgBiT at its N-terminus or SmBiT at its C-terminus,
506 respectively.

507 **Figure 3: LIT alone is not sufficient to stimulate TBK1 autophosphorylation, but**
508 **competes with WT ALTO to reduce TBK1 activation.** A) Schematic diagram of WT ALTO
509 compared to Xpress-LgBiT-Lost In Tau (LIT) expressed from the pcDNA4c vector. B) Western
510 blots of HEK 293T cells transfected with WT ALTO and LIT or matching vector controls. Primary
511 antibodies are listed on the right; left side labels differentiate multiple bands on the same blot.

512 **Figure 4: Loss of TBK1 autophosphorylation stimulatory capacity is sequence-specific.**
513 (A) Schematic diagram of tagged WT ALTO (top) and ALTO deletion of LIT (ALTOdelLIT,
514 bottom). The location of the LIT region is highlighted by a yellow box. (B) HEK 293T cells were
515 transfected with plasmids carrying either wildtype L-ALTO or L-ALTOdelLIT. Lysates were
516 harvested 24hrs post-transfection and immunoblotted with the indicated antibodies (C-F) HEK
517 293T were transfected with pairs of plasmids carrying tagged WT ALTO or ALTOdelLIT, as well
518 as tagged STING (D), Src (E), and TBK1 (F). At 20 hours (ALTO-TBK1) or 24 hours (ALTO-
519 STING and ALTO-Src) post-transfection, luminescence was measured. Points indicate biological
520 replicate wells, bars indicate means, and error bars indicate standard deviations. L-protein and
521 protein-S (and similar) indicate the named protein tagged with the LgBiT at its N-terminus or
522 SmBiT at its C-terminus, respectively. All analyses shown are Brown-Forsyth and Welch's one-
523 way ANOVA, ****$p<0.0001$; ***$p<0.001$; **$p<0.01$; *$p<0.05$

524 **Figure 5: WT ALTO and ALTOdelLIT traffic through the Golgi.** (A) inALTO and inALTOdelLIT
525 HDFs induced for 4 hours prior to fixation and immunofluorescent stained for ALTO and the cis-
526 Golgi marker GM130. (B) Representative immunofluorescence images of inALTO and
527 inALTOdelLIT HDFs fixed at 16 hours post-induction and stained for ALTO and the early
528 endosome marker Rab5.

529 **Figure 6: The LIT domain is essential for ALTO-mediated suppression of MCPyV**
530 **replication in infected cells.** (A) Western blots of HDFs inducibly expressing ALTOdelLIT or
531 WT ALTO. Lysates were collected 16 h post-induction. (B) qPCR analysis of viral DNA extracted
532 5 days post-infection from HDFs inducibly expressing WT ALTO or ALTOdelLIT, following
533 infection with equal titers of $ALTO_{null}$ MCPyV. Analysis is normalized to cellular GAPDH for each
534 cell type. Points represent biological replicate wells averaged from three technical replicates
535 each. Analyses are multiple unpaired t-tests with Welch's correction, *$p<0.05$. (C) Predicted
536 tertiary structure modeling of the ALTO/STING/TBK1/Src complex, with the LIT domain
537 highlighted at center. Full-length canonical amino acid sequences for each protein were used
538 with AlphaFold3 server (update 2025.06.10) with no post-translational modifications, default
539 parameters, random seeding.

540 **Figure S1: Predictive tertiary structures of progressive ALTO truncation mutants.** Amino
541 acid sequences of progressive ALTO truncation mutants were used with the 2025.5.23 Update
542 of the AlphaFold3 server platform (default settings, random seeding). All structures have a low-
543 confidence intrinsically disordered N-terminal region, and a relatively higher-confidence C-
544 terminal alpha helical structure, which is maintained through all truncations. All progressive
545 ALTO truncations are shown in (A) monomeric, (B) homodimeric, and (C) WT ALTO-paired
546 heterodimeric forms. Colors indicate AlphaFold calculated predicted local distance difference
547 test (plDDT) confidence scores according to the supplied key in (A).

548 **Figure S2: Progressive ALTO truncation mutants retain homo-and hetero-oligomerization**
549 **potential.** Representative NanoBiT luminescence readings of HEK 293T cells transfected with
550 pairs of plasmids carrying NanoBiT-tagged WT ALTO or a truncation mutant, or the Small BiT
551 negative control construct. Luminescence was measured at 24hrs post-transfection and
552 reported in Relative Luminescence Units (RLU). Points indicate biological replicate wells, bars
553 indicate means, and error bars indicate standard deviations. L-protein and protein-S (and

554 similar) indicate the named protein tagged with the LgBiT at its N-terminus or SmBiT at its C-
555 terminus, respectively.

556 **Figure S3: Kinetic curves of progressive ALTO truncation mutant interactions show**
557 **relative interaction stability over time.** Kinetic luminescence readings of HEK 293T cells
558 20hrs (ALTO-TBK1) or 24hrs (ALTO-STING and ALTO-Src) post-transfection with the indicated
559 NanoBiT interaction pairs. Cells were monitored for 90 minutes after the addition of substrate,
560 with readings recorded every 15min to determine the intensity and stability of protein-protein
561 interactions. Individual points reflect average values of biological replicate wells; error bars
562 indicate standard deviation across replicates at each time point; and trendlines indicate change
563 between averages across timepoints. Single representative timepoints are highlighted in
564 corresponding figures in Fig. 2.

565 **Figure S4: Protein expression in LgBiT-LIT NanoBiT experiments is not sufficiently equal**
566 **to WT to draw reliable interaction conclusions**. Western blots and representative NanoBiT
567 readings of HEK 293T cells co-transfected with tagged LIT and (A) WT ALTO, (B) STING, (C)
568 Src, and (D) TBK1 at 20 hours (TBK1) or 24 hours (all others) post-transfection. Overexposed
569 L-WT bands in (B) were covered to image the L-LIT bands (inset). Primary antibodies are
570 indicated on the right; left-side labels differentiate bands visualized on the same blot.

571 **Figure S5: ALTO150 is not sufficient to stimulate TBK1 autophosphorylation but is a**
572 **partial dominant-negative.** (A) Schematic diagram of LgBiT-tagged WT ALTO and 6* His-
573 Xpress-tagged ALTO150 as expressed from the pcDNA4c vector (B) Western blots of lysates
574 from HEK 293T cells 24 hours post-transfection with WT ALTO, ALTO150, or both. Right side
575 labels indicate primary antibodies; left side labels distinguish multiple bands on the same blot.

576 **Figure S6: Relatively equal protein expression across variants in ALTOdelLIT NanoBiT**
577 **experiments supports functional conclusions.** Western blots of lysates from HEK 293T cells

578 transfected with indicated NanoBiT pairs, corresponding to Fig. 4. Lysates were harvested at
579 20hrs (ALTO-TBK1) or 24hrs (all others) post-transfection to assess relative protein expression
580 at the time of luminescence readings. Primary antibodies are listed on the right; labels on the
581 left differentiate multiple bands on the same blot.

582 **Figure S7: SLiMs do not explain the loss of function in ALTOdelLIT.** Full-length amino acid
583 sequence of ALTO was submitted to the ELM database (elm.eu.org) functional search prediction
584 (cell compartment not specified, default parameters, Homo sapiens species context). Results
585 have been filtered to display only motifs which are present within or immediately adjacent to the
586 LIT domain. Probabilities provided by the ELM database reflect the likelihood of the motif to
587 appear by random in any given protein sequence.

588 **Figure S8: Longitudinal trafficking of WT ALTO and ALTOdelLIT.** Representative
589 immunofluorescence images of inALTO and inALTOdelLIT HDFs fixed at the indicated
590 timepoints post-induction. All images taken with the 60x objective unless otherwise indicated.
591 The WT cell shown at 100x at T=10 (white arrow) was particularly noteworthy for the apparent
592 visualization of ALTO punctae leaving the Golgi.

593 References:

594 1. Moens U C-SS, Lauber C, Ramqvist T, Feltkamp MCW, Daugherty MD, Verschoor EJ,
595 Ehlers B, and ICTV Report Consortium. 2017. ICTV Virus Taxonomy Profile:
596 Polyomaviridae. J Gen Virol.

597 2. Fazeli MM, Heydari Sirat S, Shatizadeh Malekshahi S. 2025. Novel Human
598 Polyomaviruses Discovered From 2007 to the Present: An Update of Current
599 Knowledge. Rev Med Virol 35.

600 3. Feng H, Shuda M, Chang Y, Moore PS. 2008. Clonal integration of a polyomavirus in
601 human Merkel cell carcinoma. Science 319:1096-100.

602 4. Tolstov Y. 2011. Asymptomatic Primary Merkel Cell Polyomavirus Infection among
603 Adults. Emerg Infect Dis doi:10.3201/eid1708.110079:1371-1380.

604 5. Schowalter RM, Pastrana DV, Pumphrey KA, Moyer AL, Buck CB. 2010. Merkel cell
605 polyomavirus and two previously unknown polyomaviruses are chronically shed from
606 human skin. Cell Host Microbe 7:509-15.

607 6. Tolstov YL, Pastrana DV, Feng H, Becker JC, Jenkins FJ, Moschos S, Chang Y, Buck
608 CB, Moore PS. 2009. Human Merkel cell polyomavirus infection II. MCV is a common
609 human infection that can be detected by conformational capsid epitope immunoassays.
610 Int J Cancer 125:1250-6.

611 7. Foulongne V, Kluger N, Dereure O, Mercier G, Molès J-P, Guillot B, Segondy M. 2010.
612 Merkel Cell Polyomavirus in Cutaneous Swabs. Emerg Infect Dis 16:685-687.

613 8. Bopp L, Wieland U, Hellmich M, Kreuter A, Pfister H, Silling S. 2021. Natural History of
614 Cutaneous Human Polyomavirus Infection in Healthy Individuals. Front Microbiol 12.

615 9. Chang Y, Moore PS. 2012. Merkel Cell Carcinoma: A Virus-Induced Human Cancer.
616 Annu Rev Pathol 7:123-144.

617 10. Busam KJ, Jungbluth AA, Rekthman N, Coit D, Pulitzer M, Bini J, Arora R, Hanson NC,
618 Tassello JA, Frosina D, Moore P, Chang Y. 2009. Merkel cell polyomavirus expression in

619 merkel cell carcinomas and its absence in combined tumors and pulmonary
620 neuroendocrine carcinomas. Am J Surg Pathol 33:1378-85.
621 11. Kassem A, Schopflin A, Diaz C, Weyers W, Stickeler E, Werner M, Zur Hausen A. 2008.
622 Frequent detection of Merkel cell polyomavirus in human Merkel cell carcinomas and
623 identification of a unique deletion in the VP1 gene. Cancer Res 68:5009-13.
624 12. Rodig SJ, Cheng J, Wardzala J, DoRosario A, Scanlon JJ, Laga AC, Martinez-
625 Fernandez A, Barletta JA, Bellizzi AM, Sadasivam S, Holloway DT, Cooper DJ, Kupper
626 TS, Wang LC, DeCaprio JA. 2012. Improved detection suggests all Merkel cell
627 carcinomas harbor Merkel polyomavirus. J Clin Invest 122:4645-53.
628 13. Rapchak K, Yagobian SD, Moore J, Khattri M, Shuda M. 2022. Merkel cell polyomavirus
629 small T antigen is a viral transcription activator that is essential for viral genome
630 maintenance. PLoS Pathog 18:e1011039.
631 14. Shuda M, Feng H, Kwun HJ, Rosen ST, Gjoerup O, Moore PS, Chang Y. 2008. T antigen
632 mutations are a human tumor-specific signature for Merkel cell polyomavirus. Proc Natl
633 Acad Sci U S A 105:16272-16277.
634 15. Googins MR, An P, Gauthier CH, Pipas JM. 2025. Polyomavirus large T antigens:
635 Unraveling a complex interactome. Tumour Virus Res 19:200306.
636 16. Engels EA, Frisch M, Goedert JJ, Biggar RJ, Miller RW. 2002. Merkel cell carcinoma and
637 HIV infection. Lancet 359:497-498.
638 17. Wieland U, Kreuter A. 2011. Merkel cell polyomavirus infection and Merkel cell
639 carcinoma in HIV-positive individuals. Curr Opin Oncol 23:488-493.
640 18. Ma J, Brewer J. 2014. Merkel Cell Carcinoma in Immunosuppressed Patients. Cancers
641 6:1328-1350.
642 19. Burdette DL, Monroe KM, Sotelo-Troha K, Iwig JS, Eckert B, Hyodo M, Hayakawa Y,
643 Vance RE. 2011. STING is a direct innate immune sensor of cyclic di-GMP. Nature
644 478:515-518.

645 20. Yum S, Li M, Fang Y, Chen ZJ. 2021. TBK1 recruitment to STING activates both IRF3
646 and NF-κB that mediate immune defense against tumors and viral infections. Proc Natl
647 Acad Sci U S A 118:e2100225118.
648 21. Shang G, Zhang C, Chen ZJ, Bai X-C, Zhang X. 2019. Cryo-EM structures of STING
649 reveal its mechanism of activation by cyclic GMP–AMP. Nature 567:389-393.
650 22. Jiang M, Chen P, Wang L, Li W, Chen B, Liu Y, Wang H, Zhao S, Ye L, He Y, Zhou C.
651 2020. cGAS-STING, an important pathway in cancer immunotherapy. J Hematol Oncol
652 13.
653 23. Hopfner K-P, Hornung V. 2020. Molecular mechanisms and cellular functions of cGAS–
654 STING signalling. Nat Rev Mol Cell Biol 21:501-521.
655 24. Abe T, Harashima A, Xia T, Konno H, Konno K, Morales A, Ahn J, Gutman D, Glen.
656 2013. STING Recognition of Cytoplasmic DNA Instigates Cellular Defense. Mol Cell
657 50:5-15.
658 25. Ahn J, Konno H, Barber GN. 2015. Diverse roles of STING-dependent signaling on the
659 development of cancer. Oncogene 34:5302-5308.
660 26. Liu W, Kim GB, Krump NA, Zhou Y, Riley JL, You J. 2020. Selective reactivation of
661 STING signaling to target Merkel cell carcinoma. Proc Natl Acad Sci U S A 117:13730-
662 13739.
663 27. Krump NA, Wang R, Liu W, Yang JF, Ma T, You J. 2021. Merkel Cell Polyomavirus
664 Infection Induces an Antiviral Innate Immune Response in Human Dermal Fibroblasts. J
665 Virol 95:e0221120.
666 28. Wang R, Yang JF, Senay TE, Liu W, You J. 2023. Characterization of the Impact of
667 Merkel Cell Polyomavirus-Induced Interferon Signaling on Viral Infection. J Virol
668 97:e01907-22.

669 29. Wang R, Senay TE, Luo TT, Liu W, Regan JM, Salisbury NJH, Galloway DA, You J.
670 2024. Merkel cell polyomavirus protein ALTO modulates TBK1 activity to support
671 persistent infection. PLoS Pathog 20:e1012170.
672 30. Carter JJ, Daugherty MD, Qi X, Bheda-Malge A, Wipf GC, Robinson K, Roman A, Malik
673 HS, Galloway DA. 2013. Identification of an overprinting gene in Merkel cell
674 polyomavirus provides evolutionary insight into the birth of viral genes. Proceedings of
675 the National Academy of Sciences U S A 110:12744-12749.
676 31. Peng WY, Abere B, Shi H, Toland S, Smithgall TE, Moore PS, Chang Y. 2023.
677 Membrane-bound Merkel cell polyomavirus middle T protein constitutively activates
678 PLCgamma1 signaling through Src-family kinases. Proc Natl Acad Sci U S A
679 120:e2316467120.
680 32. Salisbury NJH, Amonkar S, Landazuri Vinueza J, Carter JJ, Roman A, Galloway DA.
681 2024. Polyomavirus ALTOs, but not MTs, downregulate viral early gene expression by
682 activating the NF-kappaB pathway. Proc Natl Acad Sci U S A 121:e2403133121.
683 33. Lanclos N, Radulovic P, Bland J, Oganisyan V, Radefeld K, Uversky VN. 2024.
684 Implications of intrinsic disorder and functional proteomics in the merkel cell
685 polyomavirus life cycle. J Cell Biochem 125.
686 34. Jumper J, Evans R, Pritzel A, Green T, Figurnov M, Ronneberger O, Tunyasuvunakool
687 K, Bates R, Žídek A, Potapenko A, Bridgland A, Meyer C, Kohl SAA, Ballard AJ, Cowie
688 A, Romera-Paredes B, Nikolov S, Jain R, Adler J, Back T, Petersen S, Reiman D, Clancy
689 E, Zielinski M, Steinegger M, Pacholska M, Berghammer T, Bodenstein S, Silver D,
690 Vinyals O, Senior AW, Kavukcuoglu K, Kohli P, Hassabis D. 2021. Highly accurate
691 protein structure prediction with AlphaFold. Nature 596:583-589.
692 35. Mirdita M, Schütze K, Moriwaki Y, Heo L, Ovchinnikov S, Steinegger M. 2022.
693 ColabFold: making protein folding accessible to all. Nat Methods 19:679-682.

694 36. Dyson HJ, Wright PE. 2005. Intrinsically unstructured proteins and their functions. Nat
695 Rev Mol Cell Biol 6:197-208.
696 37. Wright PE, Dyson HJ. 1999. Intrinsically unstructured proteins: re-assessing the protein
697 structure-function paradigm. J Mol Biol 293:321-331.
698 38. Cortese MS, Uversky VN, Dunker AK. 2008. Intrinsic disorder in scaffold proteins:
699 getting more from less. Prog Biophys Mol Biol 98:85-106.
700 39. Holehouse AS, Kragelund BB. 2024. The molecular basis for cellular function of
701 intrinsically disordered protein regions. Nat Rev Mol Cell Biol 25:187-211.
702 40. Liu W, Yang R, Payne AS, Schowalter RM, Spurgeon ME, Lambert PF, Xu X, Buck CB,
703 You J. 2016. Identifying the Target Cells and Mechanisms of Merkel Cell Polyomavirus
704 Infection. Cell Host Microbe 19:775-87.
705 41. Lee J-O, Russo AA, Pavletich NP. 1998. Structure of the retinoblastoma tumour-
706 suppressor pocket domain bound to a peptide from HPV E7. Nature 391:859-865.
707 42. Majerciak V, Pripuzova N, Chan C, Temkin N, Specht SI, Zheng Z-M. 2015. Stability of
708 Structured Kaposi's Sarcoma-Associated Herpesvirus ORF57 Protein Is Regulated by
709 Protein Phosphorylation and Homodimerization. J Virol 89:3256-3274.
710 43. Dyson HJ. 2023. Vital for Viruses: Intrinsically Disordered Proteins. J Mol Biol
711 435:167860.
712 44. Mishra PM, Verma NC, Rao C, Uversky VN, Nandi CK. 2020. Intrinsically disordered
713 proteins of viruses: Involvement in the mechanism of cell regulation and pathogenesis.
714 Prog Mol Biol Transl Sci 174:1-78.
715 45. Kast-Woelbern H, Martinho SK, Julio KT, Vazzana AM, Mandagie AE, Jansma AL. 2025.
716 The Use of Intrinsic Disorder and Phosphorylation by Oncogenic Viral Proteins to
717 Dysregulate the Host Cell Cycle Through Interaction with pRb. Viruses 17:835.

718 46. Xiang S, Song S, Tang H, Smaill JB, Wang A, Xie H, Lu X. 2021. TANK-binding kinase 1
719 (TBK1): An emerging therapeutic target for drug discovery. Drug Discov Today 26:2445-
720 2455.
721 47. Sun Y, Revach O-Y, Anderson S, Kessler EA, Wolfe CH, Jenney A, Mills CE, Robitschek
722 EJ, Davis TGR, Kim S, Fu A, Ma X, Gwee J, Tiwari P, Du PP, Sindurakar P, Tian J,
723 Mehta A, Schneider AM, Yizhak K, Sade-Feldman M, Lasalle T, Sharova T, Xie H, Liu S,
724 Michaud WA, Saad-Beretta R, Yates KB, Iracheta-Vellve A, Spetz JKE, Qin X, Sarosiek
725 KA, Zhang G, Kim JW, Su MY, Cicerchia AM, Rasmussen MQ, Klempner SJ, Juric D, Pai
726 SI, Miller DM, Giobbie-Hurder A, Chen JH, Pelka K, Frederick DT, Stinson S, Ivanova E,
727 Aref AR, Paweletz CP, Barbie DA, et al. 2023. Targeting TBK1 to overcome resistance to
728 cancer immunotherapy. Nature 615:158-167.
729 48. Sun Y, Maggs L, Panda A, Wright SJ, Cicerchia AM, Jenney A, Perricone MD, Mills CE,
730 Cattaneo G, Ventin M, Chen F, Rasmussen MQ, Miranda A, Revach O-Y, Fang J, Fu A,
731 Bowling PJ, Sharova T, Lawless A, Sorger PK, Bardeesy N, Wang X, Flaherty KT,
732 Boland GM, Mehta A, Sade-Feldman M, Ferrone CR, Jenkins RW. 2025. TBK1 Targeting
733 Is Identified as a Therapeutic Strategy to Enhance CAR T-Cell Efficacy Using Patient-
734 Derived Organotypic Tumor Spheroids. Cancer Immunol Res 13:210-228.
735 49. Liu W, Krump NA, Buck CB, You J. 2019. Merkel Cell Polyomavirus Infection and
736 Detection. J Vis Exp doi:10.3791/58950.
737 50. Wang J, Youkharibache P, Zhang D, Lanczycki CJ, Geer RC, Madej T, Phan L, Ward M,
738 Lu S, Marchler GH, Wang Y, Bryant SH, Geer LY, Marchler-Bauer A. 2020. iCn3D, a
739 web-based 3D viewer for sharing 1D/2D/3D representations of biomolecular structures.
740 Bioinformatics 36:131-135.
741 51. Wang J, Youkharibache P, Marchler-Bauer A, Lanczycki C, Zhang D, Lu S, Madej T,
742 Marchler GH, Cheng T, Chong LC, Zhao S, Yang K, Lin J, Cheng Z, Dunn R, Malkaram
743 SA, Tai C-H, Enoma D, Busby B, Johnson NL, Tabaro F, Song G, Ge Y. 2022. iCn3D:

From Web-Based 3D Viewer to Structural Analysis Tool in Batch Mode. Front Mol Biosci 9.

Figure 1

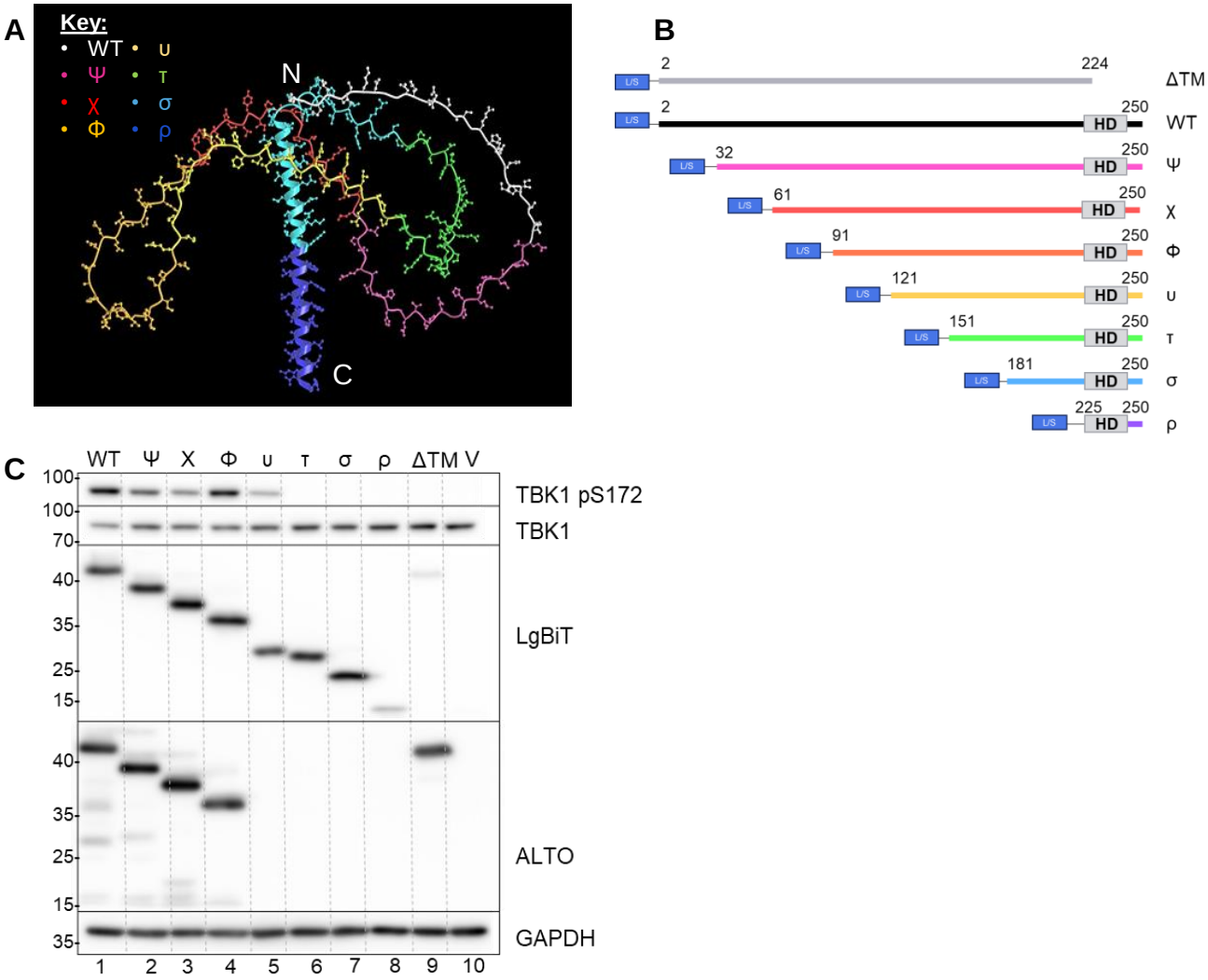
A
Key:
WT
υ
Ψ
τ
χ
σ
Φ
ρ
N
C
B
L/S
HD
2
224
ΔTM
2
250
WT
32
250
Ψ
61
250
χ
91
250
Φ
121
250
υ
151
250
τ
181
250
σ
225
250
ρ
C
WT
Ψ
X
Φ
υ
τ
σ
ρ
ΔTM
V
100
100
70
40
35
25
15
40
35
25
15
35
TBK1 pS172
TBK1
LgBiT
ALTO
GAPDH
1
2
3
4
5
6
7
8
9
10

Figure 2

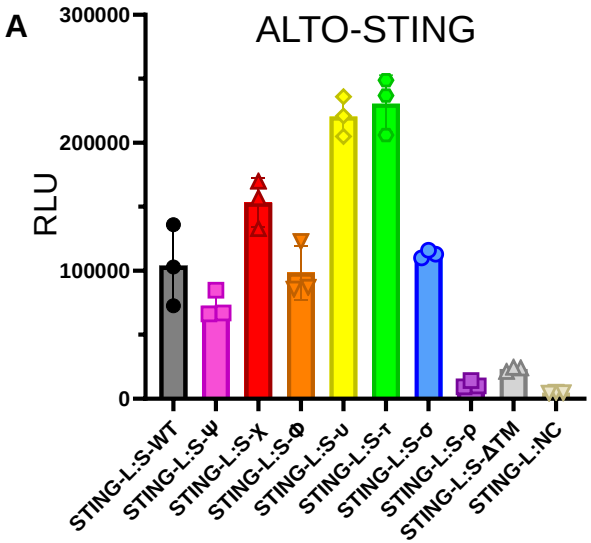
A
ALTO-STING
RLU
300000
200000
100000
0
STING-L:S-WT
STING-L:S-ψ
STING-L:S-χ
STING-L:S-Φ
STING-L:S-υ
STING-L:S-τ
STING-L:S-σ
STING-L:S-ρ
STING-L:S-ΔTM
STING-L:NC

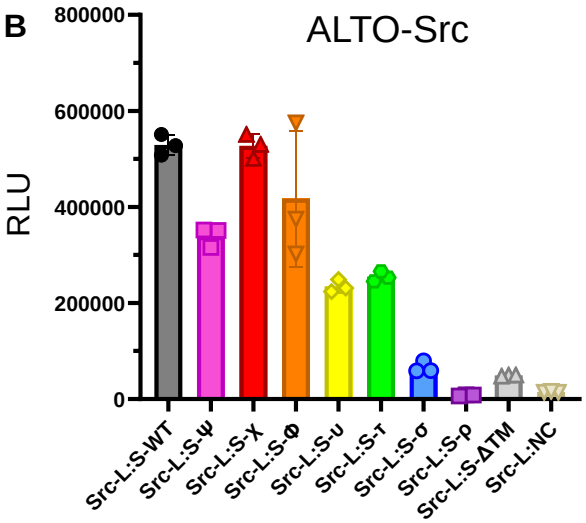
B
ALTO-Src
RLU
800000
600000
400000
200000
0
Src-L:S-WT
Src-L:S-ψ
Src-L:S-χ
Src-L:S-Φ
Src-L:S-υ
Src-L:S-τ
Src-L:S-σ
Src-L:S-ρ
Src-L:S-ΔTM
Src-L:NC

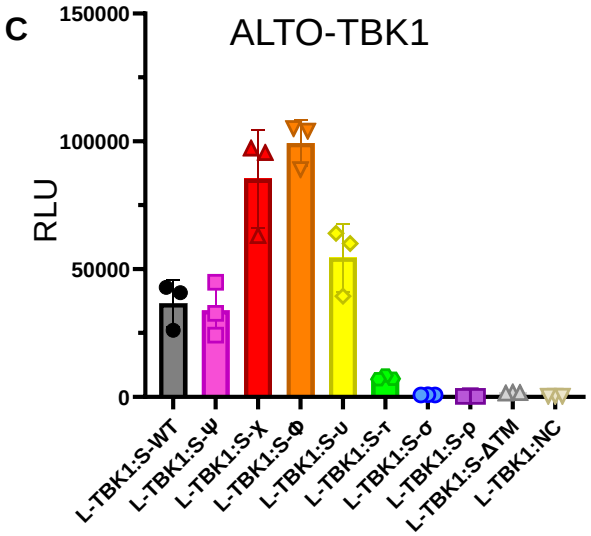
C
ALTO-TBK1
RLU
150000
100000
50000
0
L-TBK1:S-WT
L-TBK1:S-ψ
L-TBK1:S-χ
L-TBK1:S-Φ
L-TBK1:S-υ
L-TBK1:S-τ
L-TBK1:S-σ
L-TBK1:S-ρ
L-TBK1:S-ΔTM
L-TBK1:NC

Figure 3

A

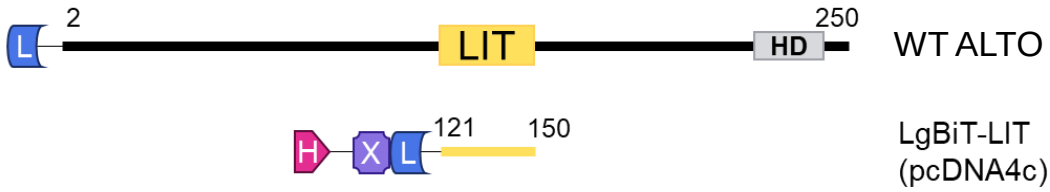
2
L
LIT
HD
250
WT ALTO
H
X
L
121
150
LgBiT-LIT
(pcDNA4c)

B

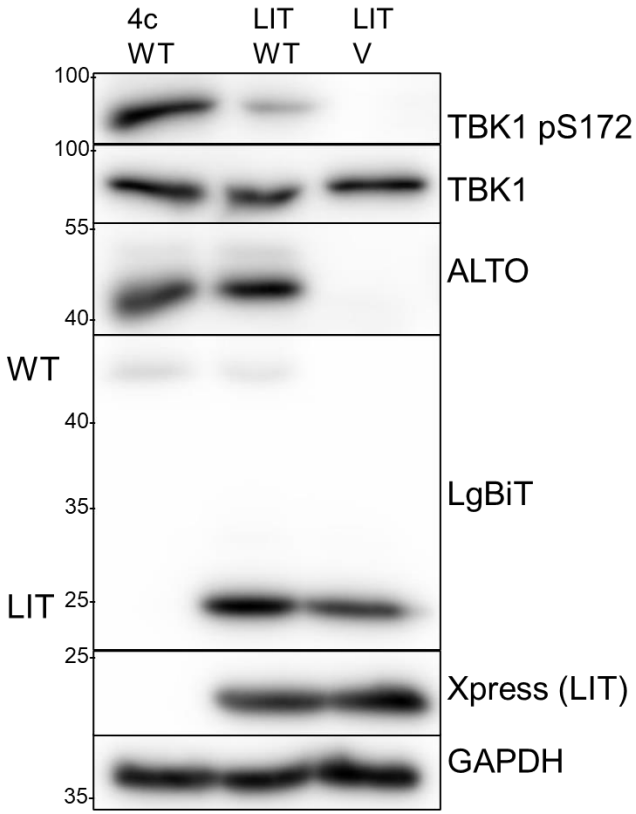
4c
WT
LIT
WT
LIT
V
100
100
55
40
40
35
25
25
35
WT
LIT
TBK1 pS172
TBK1
ALTO
LgBiT
Xpress (LIT)
GAPDH

Figure 4

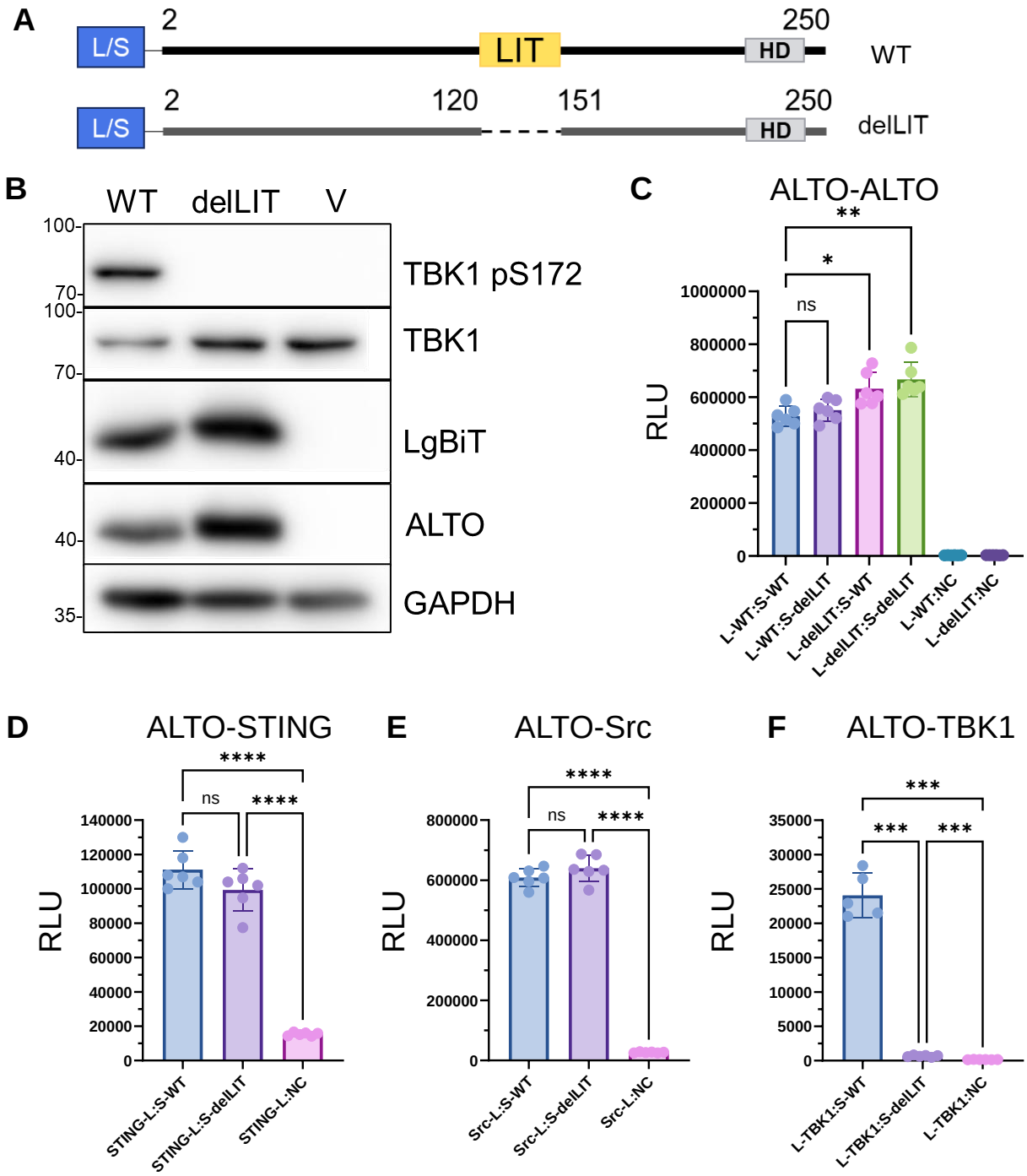
A
L/S
2
LIT
250
HD
WT
L/S
2
120
151
250
HD
delLIT
B
WT
delLIT
V
100-
70-
100-
70-
40-
40-
35-
TBK1 pS172
TBK1
LgBiT
ALTO
GAPDH
C
ALTO-ALTO
RLU
1000000
800000
600000
400000
200000
0
ns
*
**
L-WT:S-WT
L-WT:S-delLIT
L-delLIT:S-WT
L-delLIT:S-delLIT
L-WT:NC
L-delLIT:NC
D
ALTO-STING
RLU
140000
120000
100000
80000
60000
40000
20000
0
ns
****
****
STING-L:S-WT
STING-L:S-delLIT
STING-L:NC
E
ALTO-Src
RLU
800000
600000
400000
200000
0
ns
****
****
Src-L:S-WT
Src-L:S-delLIT
Src-L:NC
F
ALTO-TBK1
RLU
35000
30000
25000
20000
15000
10000
5000
0
***
***
***
L-TBK1:S-WT
L-TBK1:S-delLIT
L-TBK1:NC

Figure 5

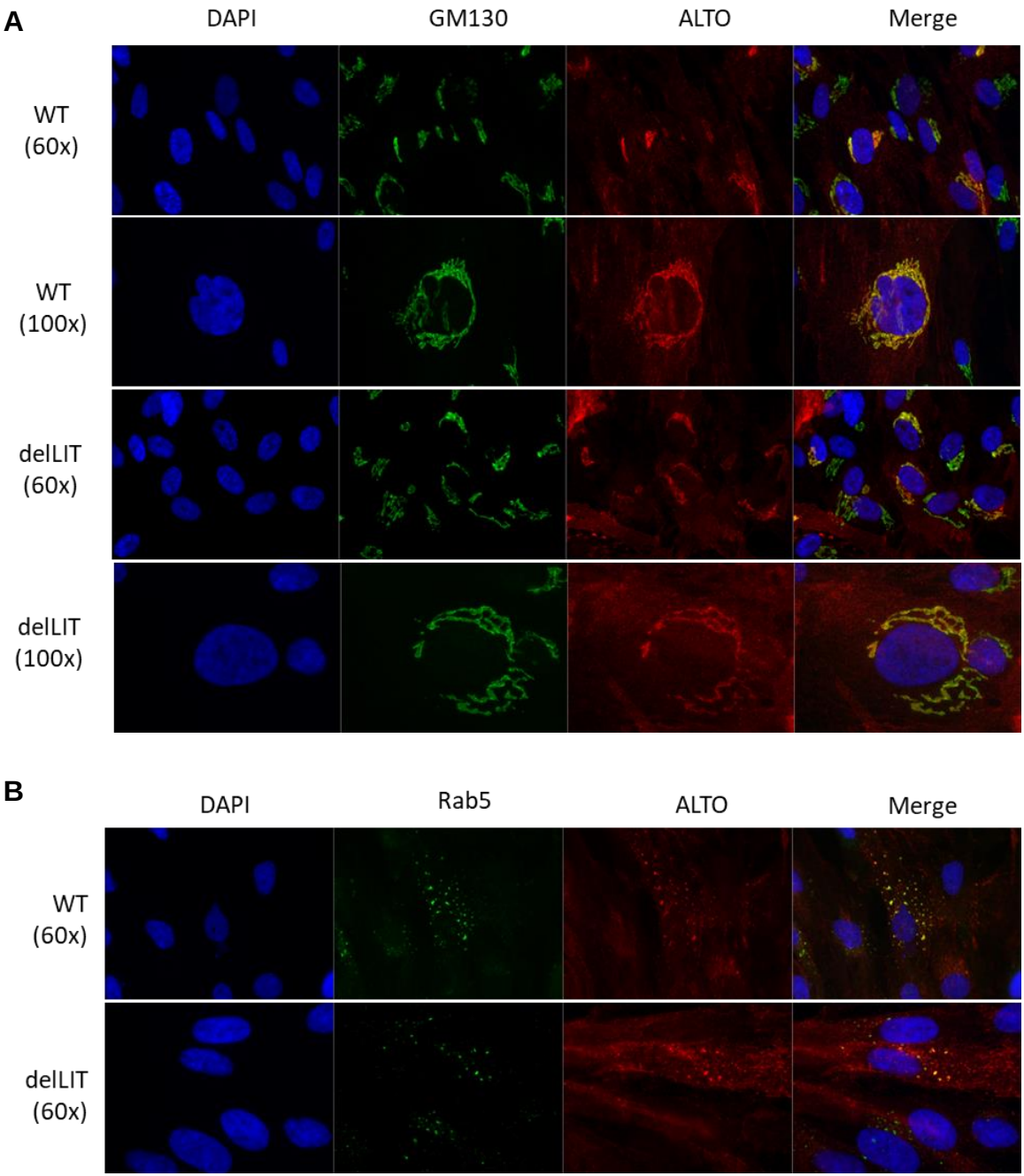
A
DAPI
GM130
ALTO
Merge
WT (60x)
WT (100x)
delLIT (60x)
delLIT (100x)
B
DAPI
Rab5
ALTO
Merge
WT (60x)
delLIT (60x)

Figure 6

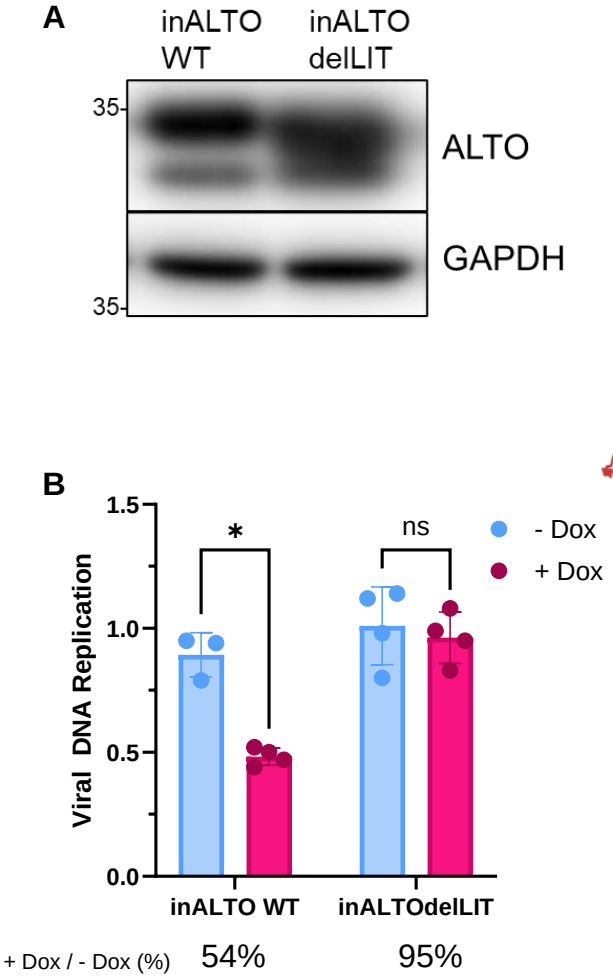
A
inALTO WT
inALTO delLIT
35
ALTO
GAPDH
35
B
1.5
1.0
0.5
0.0
Viral DNA Replication
*
ns
- Dox
+ Dox
inALTO WT
inALTOdelLIT
+ Dox / - Dox (%)
54%
95%

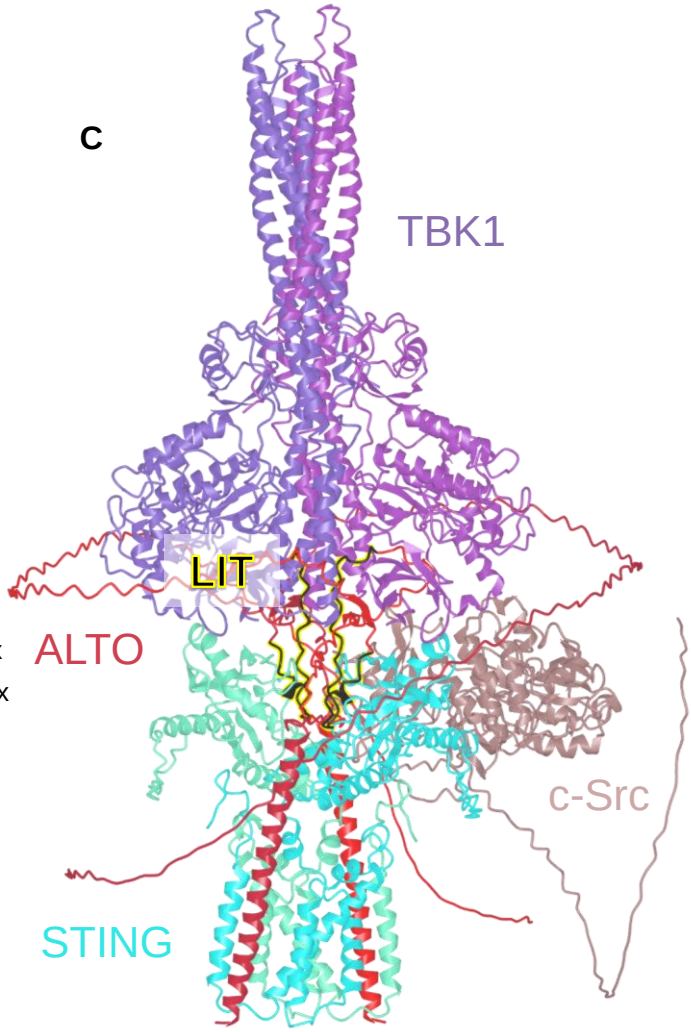
C
TBK1
LIT
ALTO
c-Src
STING

Figure S1

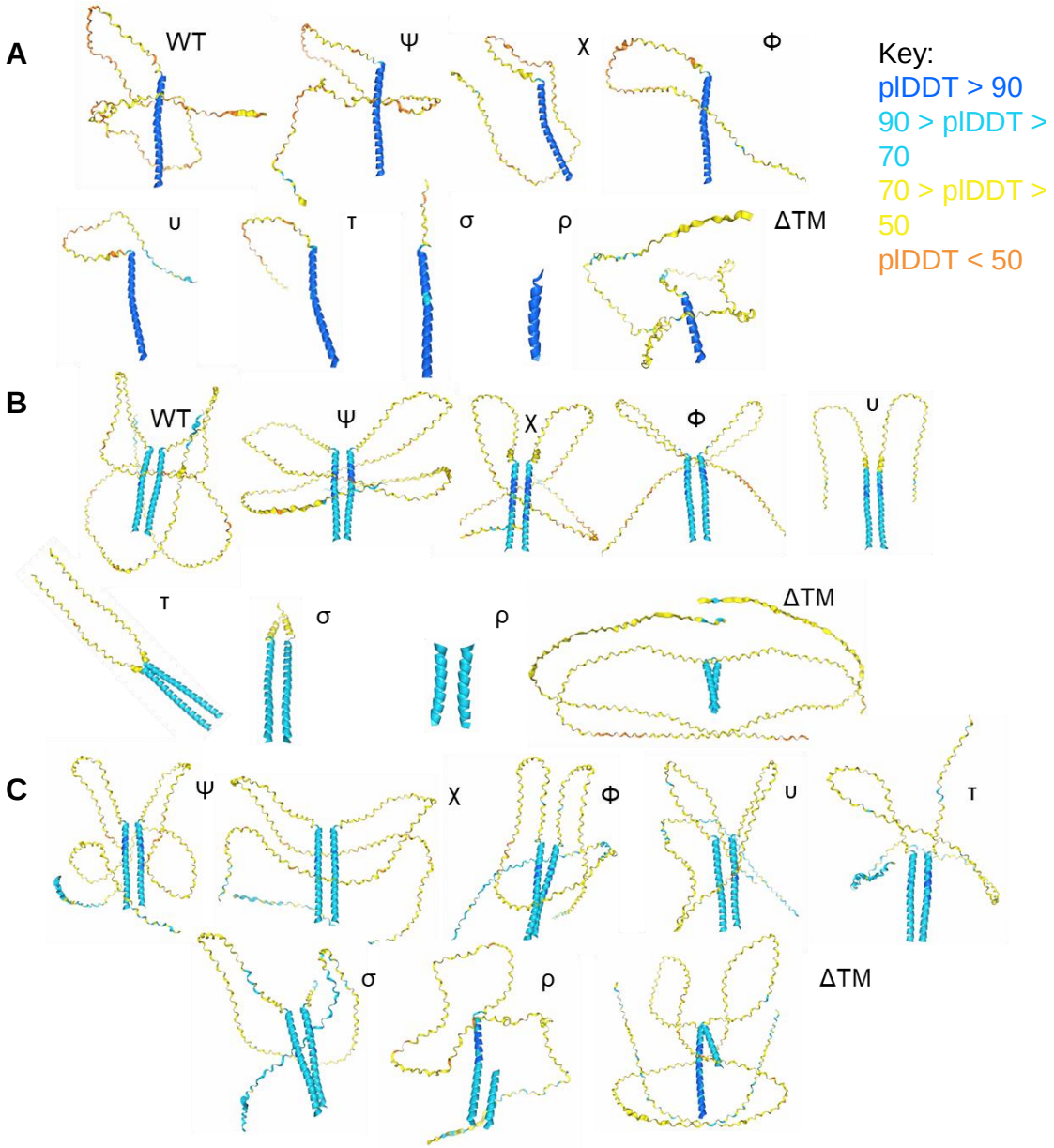
A
WT
Ψ
χ
Φ
υ
τ
σ
ρ
ΔTM
Key:
pIDDT > 90
90 > pIDDT > 70
70 > pIDDT > 50
pIDDT < 50
B
WT
Ψ
χ
Φ
υ
τ
σ
ρ
ΔTM
C
Ψ
χ
Φ
υ
τ
σ
ρ
ΔTM

Figure S2

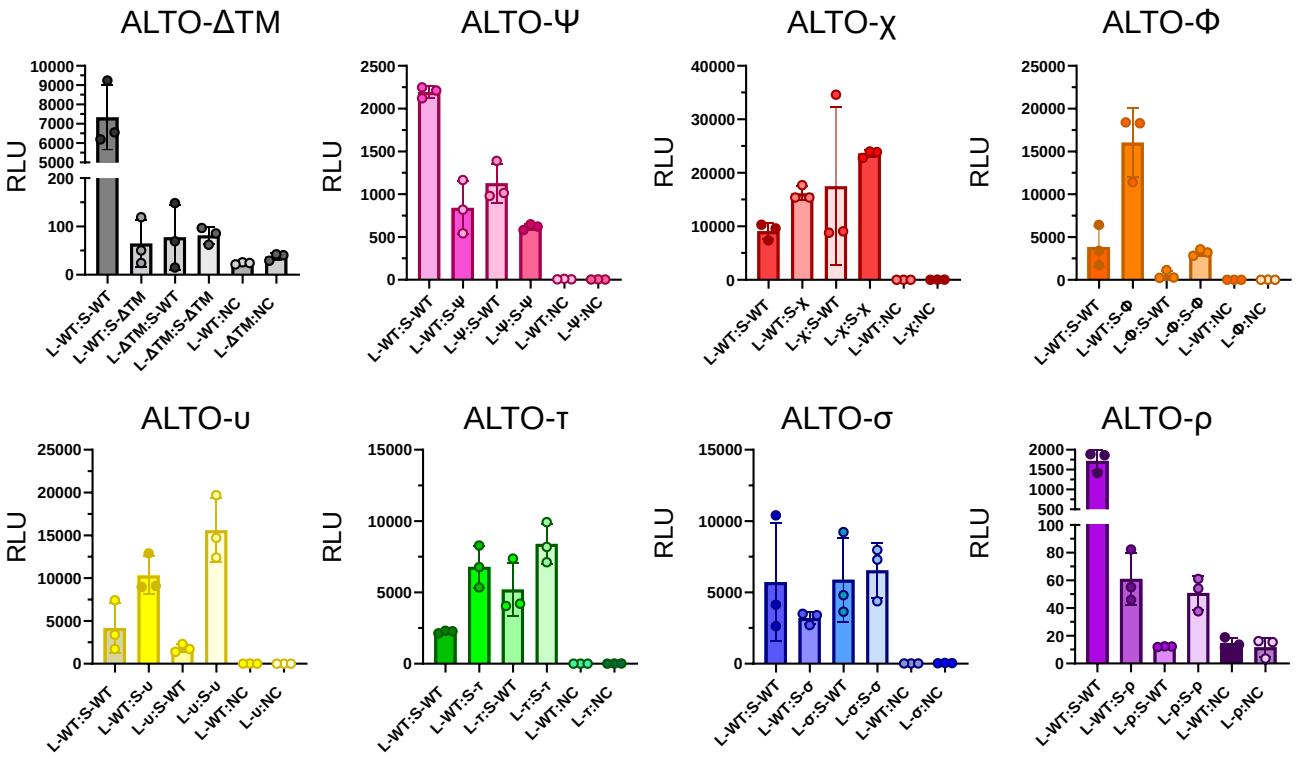
ALTO-ΔTM
RLU
L-WT:S-WT
L-WT:S-ΔTM
L-ΔTM:S-WT
L-ΔTM:S-ΔTM
L-WT:NC
L-ΔTM:NC
ALTO-Ψ
RLU
L-WT:S-WT
L-WT:S-ψ
L-ψ:S-WT
L-ψ:S-ψ
L-WT:NC
L-ψ:NC
ALTO-χ
RLU
L-WT:S-WT
L-WT:S-χ
L-χ:S-WT
L-χ:S-χ
L-WT:NC
L-χ:NC
ALTO-Φ
RLU
L-WT:S-WT
L-WT:S-Φ
L-Φ:S-WT
L-Φ:S-Φ
L-WT:NC
L-Φ:NC
ALTO-υ
RLU
L-WT:S-WT
L-WT:S-υ
L-υ:S-WT
L-υ:S-υ
L-WT:NC
L-υ:NC
ALTO-τ
RLU
L-WT:S-WT
L-WT:S-τ
L-τ:S-WT
L-τ:S-τ
L-WT:NC
L-τ:NC
ALTO-σ
RLU
L-WT:S-WT
L-WT:S-σ
L-σ:S-WT
L-σ:S-σ
L-WT:NC
L-σ:NC
ALTO-ρ
RLU
L-WT:S-WT
L-WT:S-ρ
L-ρ:S-WT
L-ρ:S-ρ
L-WT:NC
L-ρ:NC

Figure S3

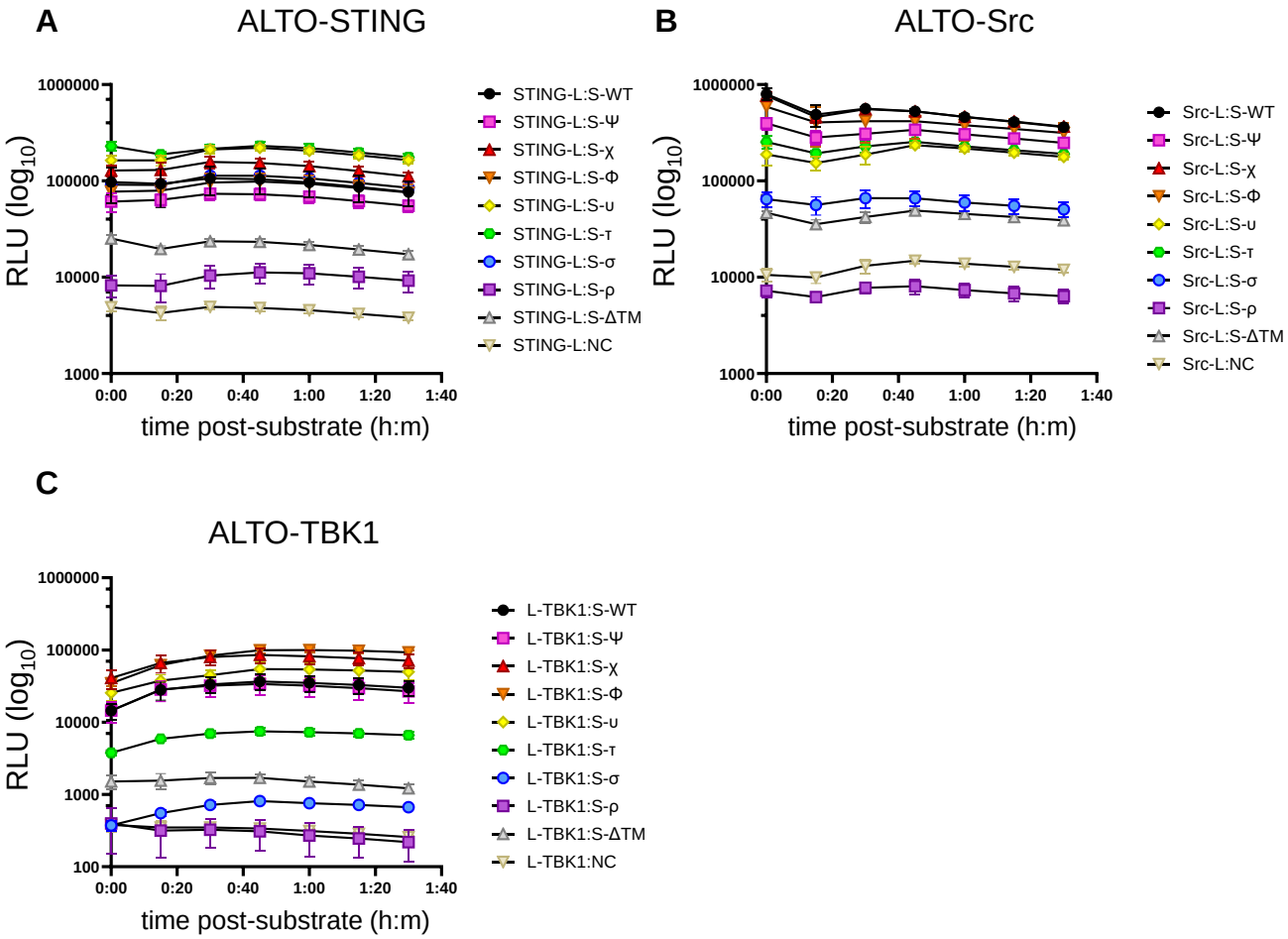
A
ALTO-STING
RLU (log10)
1000000
100000
10000
1000
0:00
0:20
0:40
1:00
1:20
1:40
time post-substrate (h:m)
STING-L:S-WT
STING-L:S-Ψ
STING-L:S-χ
STING-L:S-Φ
STING-L:S-υ
STING-L:S-τ
STING-L:S-σ
STING-L:S-ρ
STING-L:S-ΔTM
STING-L:NC
B
ALTO-Src
RLU (log10)
1000000
100000
10000
1000
0:00
0:20
0:40
1:00
1:20
1:40
time post-substrate (h:m)
Src-L:S-WT
Src-L:S-Ψ
Src-L:S-χ
Src-L:S-Φ
Src-L:S-υ
Src-L:S-τ
Src-L:S-σ
Src-L:S-ρ
Src-L:S-ΔTM
Src-L:NC
C
ALTO-TBK1
RLU (log10)
1000000
100000
10000
1000
100
0:00
0:20
0:40
1:00
1:20
1:40
time post-substrate (h:m)
L-TBK1:S-WT
L-TBK1:S-Ψ
L-TBK1:S-χ
L-TBK1:S-Φ
L-TBK1:S-υ
L-TBK1:S-τ
L-TBK1:S-σ
L-TBK1:S-ρ
L-TBK1:S-ΔTM
L-TBK1:NC

Figure S4

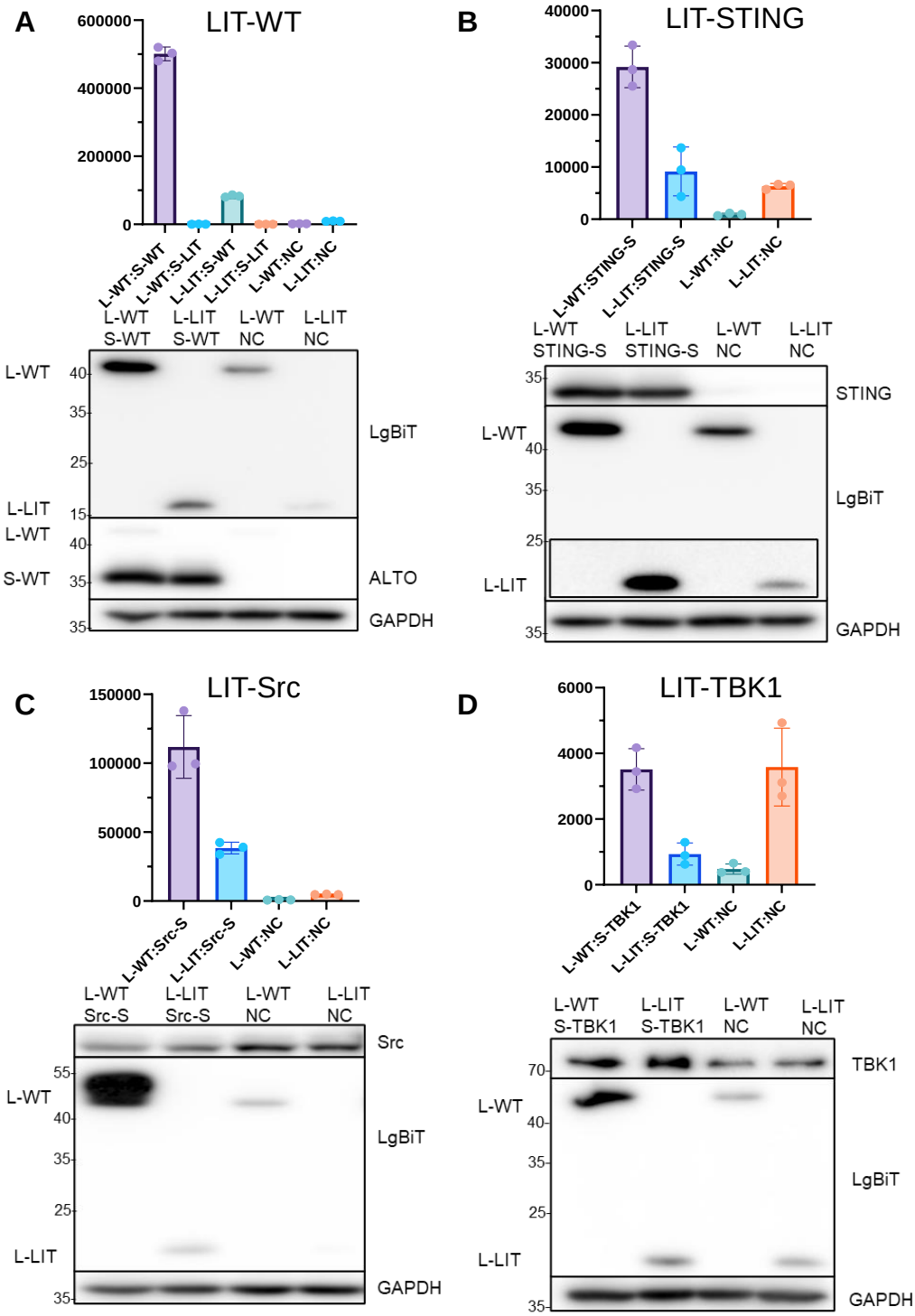
A
LIT-WT
600000
400000
200000
0
L-WT:S-WT
L-WT:S-LIT
L-LIT:S-WT
L-LIT:S-LIT
L-WT:NC
L-LIT:NC
L-WT S-WT
L-LIT S-WT
L-WT NC
L-LIT NC
L-WT
L-LIT
L-WT
S-WT
40
35
25
15
40
35
35
LgBiT
ALTO
GAPDH
B
LIT-STING
40000
30000
20000
10000
0
L-WT:STING-S
L-LIT:STING-S
L-WT:NC
L-LIT:NC
L-WT STING-S
L-LIT STING-S
L-WT NC
L-LIT NC
35
STING
L-WT
40
35
LgBiT
25
L-LIT
35
GAPDH
C
LIT-Src
150000
100000
50000
0
L-WT:Src-S
L-LIT:Src-S
L-WT:NC
L-LIT:NC
L-WT Src-S
L-LIT Src-S
L-WT NC
L-LIT NC
Src
55
L-WT
40
35
LgBiT
25
L-LIT
35
GAPDH
D
LIT-TBK1
6000
4000
2000
0
L-WT:S-TBK1
L-LIT:S-TBK1
L-WT:NC
L-LIT:NC
L-WT S-TBK1
L-LIT S-TBK1
L-WT NC
L-LIT NC
70
TBK1
L-WT
40
35
LgBiT
25
L-LIT
35
GAPDH

Figure S5

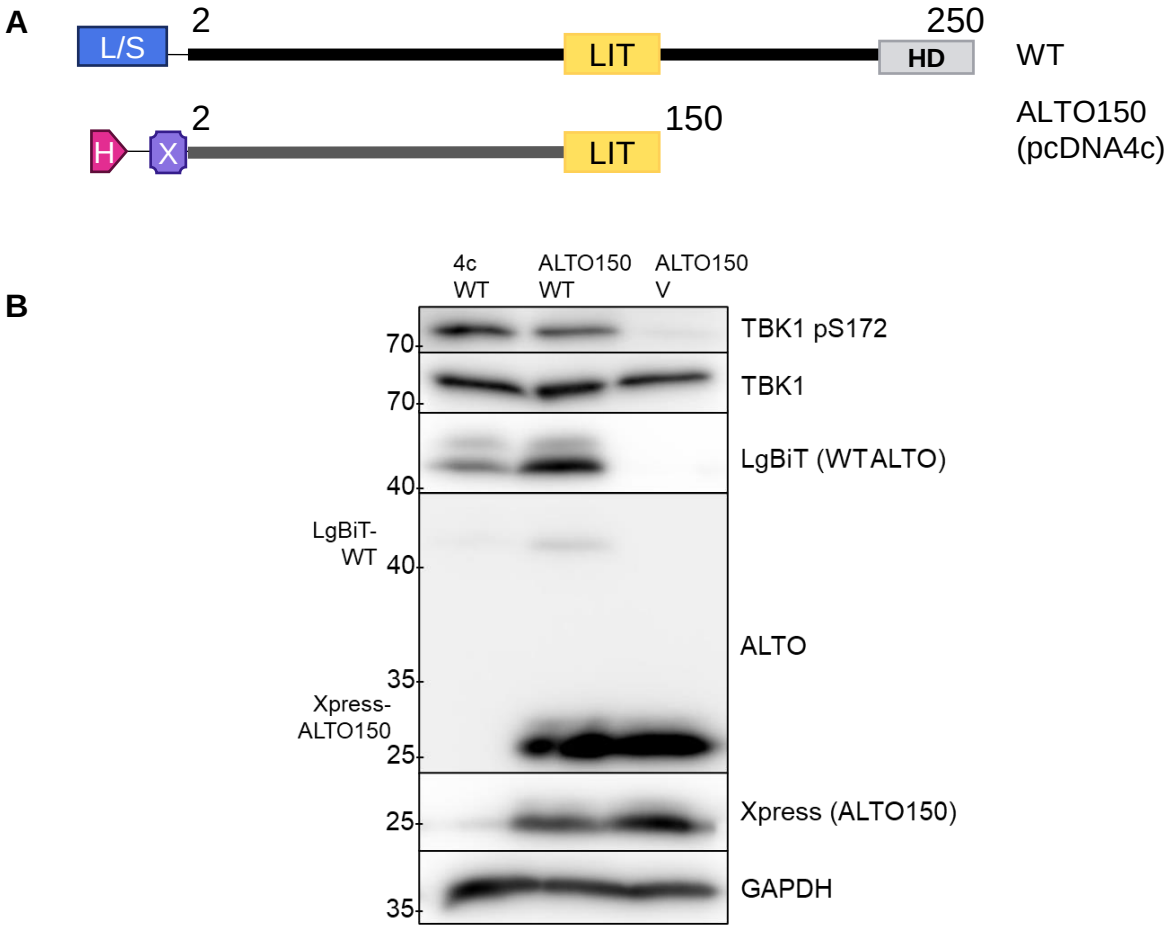
A
L/S
2
LIT
250
HD
WT
H
X
2
LIT
150
ALTO150
(pcDNA4c)
B
4c
WT
ALTO150
WT
ALTO150
V
70
TBK1 pS172
70
TBK1
40
LgBiT (WTALTO)
LgBiT-
WT
40
ALTO
35
Xpress-
ALTO150
25
25
Xpress (ALTO150)
35
GAPDH

Figure S6

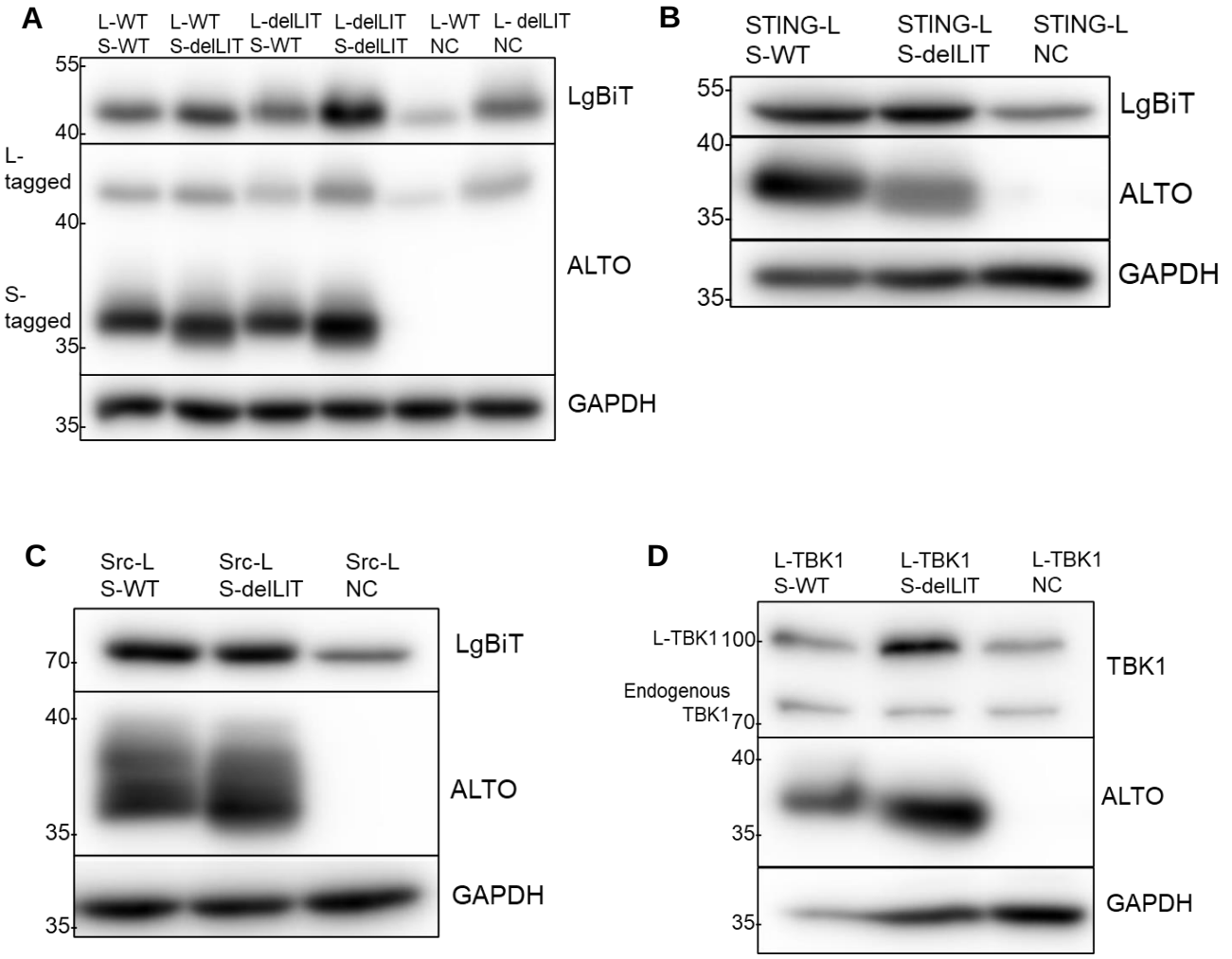
A
L-WT S-WT
L-WT S-delLIT
L-delLIT S-WT
L-delLIT S-delLIT
L-WT NC
L- delLIT NC
55
40
L-tagged
40
S-tagged
35
35
LgBiT
ALTO
GAPDH
B
STING-L S-WT
STING-L S-delLIT
STING-L NC
55
40
35
35
LgBiT
ALTO
GAPDH
C
Src-L S-WT
Src-L S-delLIT
Src-L NC
70
40
35
35
LgBiT
ALTO
GAPDH
D
L-TBK1 S-WT
L-TBK1 S-delLIT
L-TBK1 NC
L-TBK1 100
Endogenous TBK1 70
40
35
35
TBK1
ALTO
GAPDH

Figure S7

ELM Name & Description	Matched Sequence	Amino Acid Positions	Motif Type	Probability
DOC_PP2A_B56_1 Docking site for PP2A regulatory subunit B56	LEILPER	115-121	Docking	0.001458
DOC_USP7_MATH_1 USP7 MATH domain binding motif	PLRSL	142-146	Docking	0.01239
LIG_14-3-3_CanoR_1 Canonical Arg-containing phospho-motif mediating interaction with 14-3-3 proteins	RISSAMNHFP	126-135	Ligand binding	0.004477
	RPLRSLR	141-147	Ligand binding	
LIG_LIR_Gen_1 Canonical LIR motif binding to LC3 family proteins to mediate autophagy	EPVYLEILPERM	111-122	Ligand binding	0.003631
MOD_GlcNHglycn Glycosaminoglycan attachment site	SSAM	128-131	Post-translational modification	0.01792
MOD_PKA_2 Secondary preference for PKA-type AGC kinase phosphorylation	GRISSAM	125-131	Post-translational modification	0.009458
MOD_ProDKin_1 Proline-Directed Kinase phosphorylation site	SLRSPPP	145-151	Post-translational modification	0.01543

Figure S8

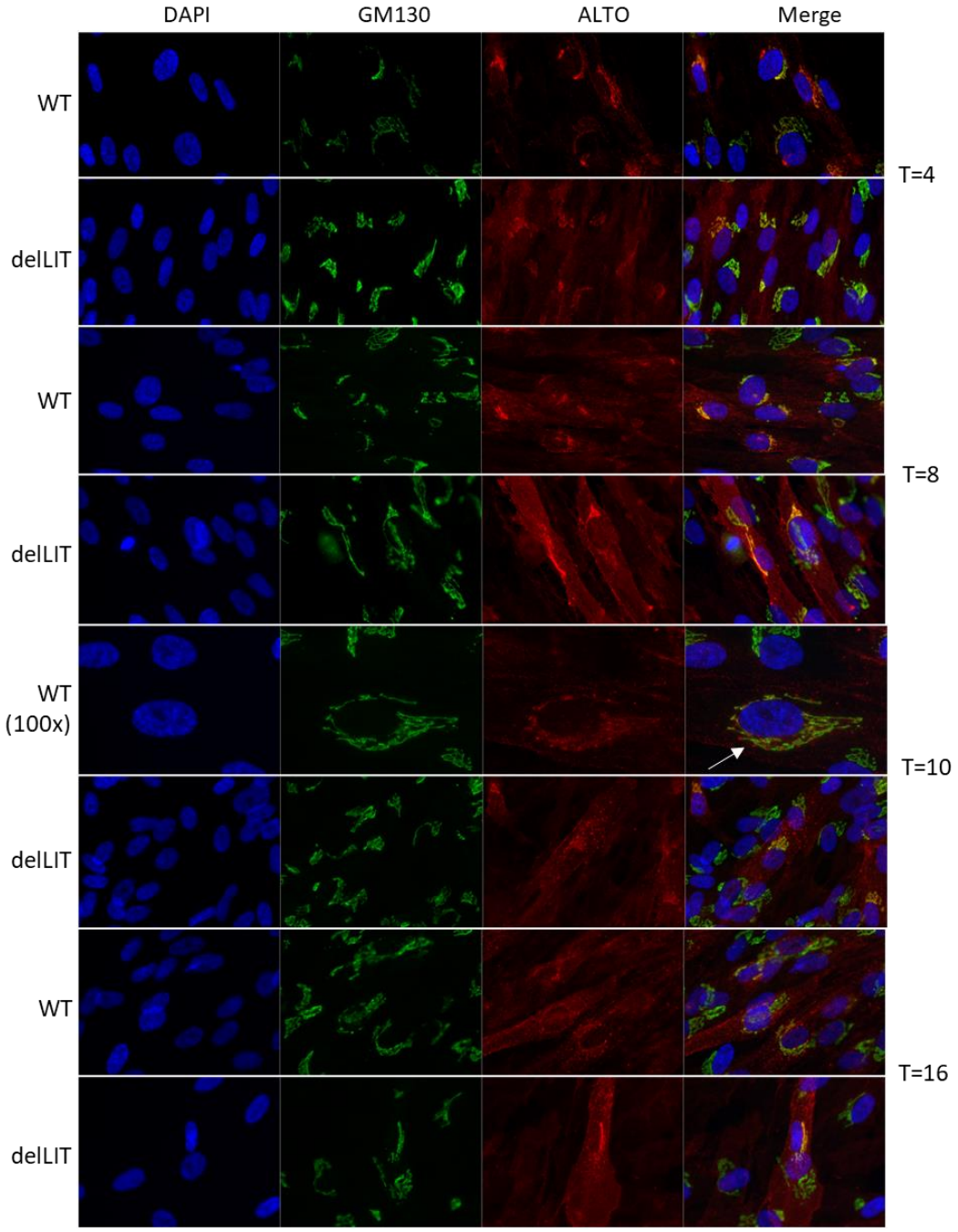
DAPI
GM130
ALTO
Merge
WT
delLIT
WT
delLIT
WT
(100x)
delLIT
WT
delLIT
T=4
T=8
T=10
T=16